Instabilities of a vortex-ring-bright soliton in trapped binary three-dimensional Bose-Einstein condensates

Victor P. Ruban, Wenlong Wang, Christopher Ticknor, and Panayotis G. Kevrekidis

Phys. Rev. A **105**, 013319 — Published 25 January 2022

DOI: 10.1103/PhysRevA.105.013319

Instabilities of vortex-ring-bright soliton in trapped binary 3D Bose-Einstein condensates

Victor P. Ruban,[1,*] Wenlong Wang,[2,†] Christopher Ticknor,[3,‡] and Panayotis G. Kevrekidis[4,§]

[1] *Landau Institute for Theoretical Physics, RAS, Chernogolovka, Moscow region 142432, Russia*
[2] *College of Physics, Sichuan University, Chengdu 610065, China*
[3] *Theoretical Division, Los Alamos National Laboratory, Los Alamos, New Mexico 87545, USA*
[4] *Department of Mathematics and Statistics, University of Massachusetts, Amherst MA 01003-4515, USA*

(Dated: January 3, 2022)

Instabilities of vortex-ring-bright coherent structures in harmonically trapped two-component three-dimensional Bose-Einstein condensates are studied numerically within the coupled Gross-Pitaevskii equations and interpreted analytically. Interestingly, the filled vortex core with a sufficiently large amount of the bright component is observed to reduce the parametric interval of stability of the vortex ring. We have identified the mechanisms of several linear instabilities and one nonlinear parametric instability in this connection. Two of the linear instabilities are qualitatively different from ones reported earlier, to our knowledge, and are associated with azimuthal modes of $m = 0$ and $m = 1$, i.e., deviations of the vortex from the stationary ring shape. Our nonlinear parametric resonance instability occurs between the $m = 0$ and $m = 2$ modes and signals the exchange of energy between them.

I. INTRODUCTION

The study of Bose-Einstein condensates (BECs) has offered for two and a half decades now an ideal playground for the exploration of nonlinear phenomena [1–3]. Specifically, the study of topological excitations has been of wide interest to the research communities of atomic, nonlinear and wave physics [4, 5]. Indeed, relevant reviews have focused not only on two-dimensional vortical structures, but also on three-dimensional vortex lines and vortex rings [6], as well as on more complex patterns including skyrmions [7–9], Dirac monopoles [10] and quantum knots [11–14].

While the majority of the studies has naturally been directed at the understanding of the single-component BEC setting, the study of multi-component BECs has also attracted considerable attention both in the two-component setting [15], but also in the case of the so-called spinor condensates [16, 17] of more than two components. Indeed, such multi-component settings have offered an ideal framework for the exploration of ideas of phase separation [18–21], but also for the manifestation of a wide range of fluid-like instabilities. The latter include, among others, the Rayleigh-Taylor instability [22–24], the Kelvin-Helmholtz instability [25–27], the capillary [28, 29] and Richtmyer-Meshkov [30] instabilities, as well as the countersuperflow [31–34], but also the Rosensweig [35] instabilities. This wealth of findings clearly illustrates the fact that multi-component systems may possess a significant additional wealth of features, in omparison with the simpler single-component ones.

It is exactly on this nexus of nonlinear topological coherent structures and their instabilities, but focusing on the multi-component variants thereof that our present study intends to focus. Earlier work of different subsets of the present authors [36–39] has explored the instabilities of chiefly one-component, three-dimensional structures, such as vortex lines and vortex rings, as well as multi-line/ring variants thereof. The last few years have led to a deeper and intensified consideration of vortical patterns bearing a second component that fills the relevant vortex core [40–43], as well as their dynamics and instabilities [44, 45], and interactions with each other [46, 47] and with defects [48]. Most of these above studies have been centered around the somewhat less computationally intensive, yet still quite interesting 2d realm. Our aim here is to extend such multi-component, filled-vortex considerations to structures arising in three-dimensional condensates. More concretely, as our prototypical example, we will explore filled-core vortex rings.

The so-called vortex-ring-bright (VRB) structures (see some numerical examples in Figs. 1 and 2) are among the canonical generalizations of the widely studied single-component vortex ring [6, 37, 39]. For the latter in our earlier work, we had explored [49] numerically the theoretically predicted instabilities [50], finding that azimuthal perturbations of different modes of azimuthal wavenumber m become unstable in different regimes of anisotropy of the condensate confinement. Indeed, for prolate BECs, the mode with $m = 1$ was found to be unstable leading to tumbling motion of the VR structure. Weakly oblate BECs represented the canonical regions of stability of the VR, while sufficiently oblate ones led to the instability, progressively of the $m = 2$, $m = 3$ etc. modes, splitting the VR into two-, three- etc. vortex lines, respectively. Here, our aim is to examine what happens to the same phenomenology, when the core of the ring vortex is filled by a second component. In line with the wealth of phenomenology identified in earlier multi-component studies, we find a variety of potential instabilities, including some that are unprecedented, to the best of our knowledge. The $m = 2$ mode instability still occurs, but at a wider range of anisotropies due to the presence of the second component. For the $m = 1$ mode, an oscillatory variant of the relevant instability is newly emergent for a suitable range of atom numbers/chemical potentials. Finally, as concerns linear instabilities, in a narrow parametric regime an unprecedented insta-

*Electronic address: ruban@itp.ac.ru
†Electronic address: wenlongcmp@scu.edu.cn
‡Electronic address: cticknor@lanl.gov
§Electronic address: kevrekid@umass.edu

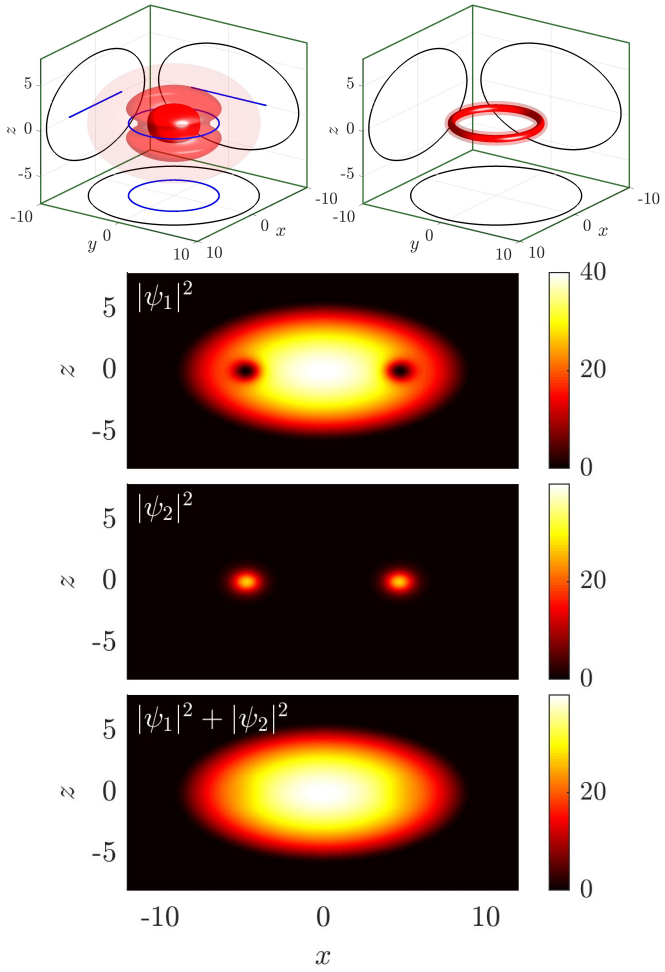

FIG. 1: A typical, numerically exact fat-core VRB configuration with a relatively massive bright component at $\kappa = 1.6, g_{12} = 1.02, \mu_1 = 40$ and $\mu_2 = 39.6$. In the top row, the density isocontours of the condensates are shown in red, and the VR core is highlighted in blue along with its projections onto the different coordinate planes. The large ellipses are projections of the Thomas-Fermi boundary. Notice how the second component bright ring overlaps with the location of the first component vortex ring, forming the VRB structure. In the second-fourth row panels, the density projections along the x-z plane are illustrated in detail. Note that the configuration is rotationally symmetric about the z-axis. The vortical (dipolar) pattern of the second row and the bright (second component) pattern of the third row add up to the total density featuring a Thomas-Fermi (TF) profile for the density equal to $\max(\mu_1 - V, 0)$ on the fourth panel.

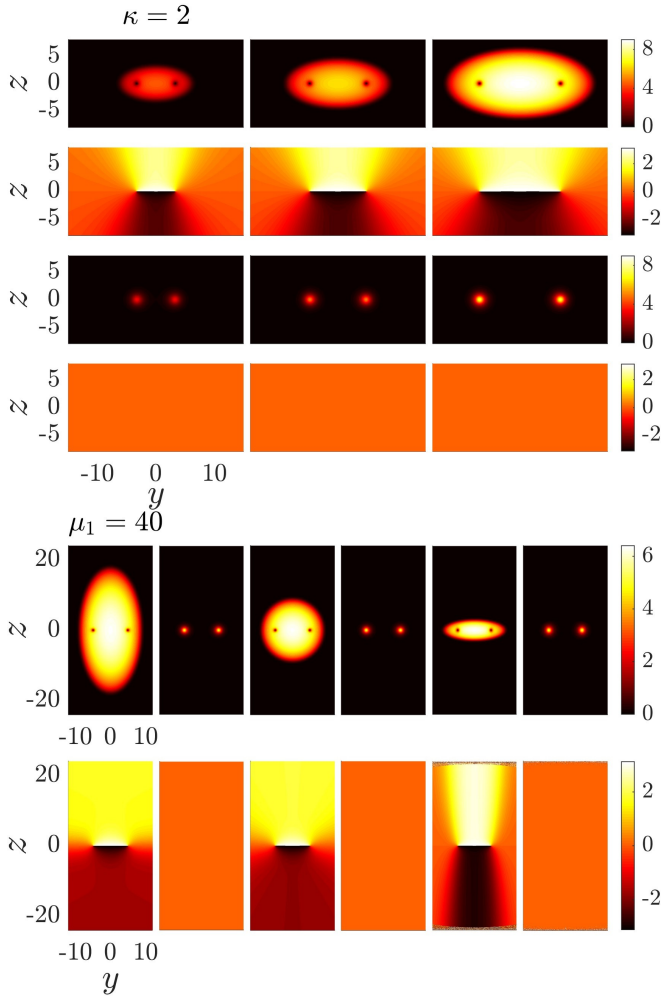

FIG. 2: Typical stationary VRB configurations: the amplitude and phase profiles are depicted in odd and even rows, respectively. In top panels, the three columns, in turn, are for chemical potentials $\mu_1 = 20, 40$ and 80 at $\kappa = 2$, see Eq. (31) for the respective values of μ_2. In the bottom panels, the state at $\mu_1 = 40$ above is continued in the aspect ratio to $\kappa = 0.5, 1$ and 3, respectively.

bility of the $m = 0$ mode is found to arise. Lastly, we also identify a nonlinear (parametric) instability stemming from the resonance between the $m = 0$ and the $m = 2$ modes, causing the exchange of energy between the two.

In what follows, our presentation of these phenomena for the VRB structures is as follows. First, we qualitatively justify theoretically the origin of these instabilities, after having presented the mathematical setup of our work. Then we present our computational setup, and in Sec. IV, we support our theoretical analysis by means of numerical computations of existence, stability and dynamics of VRB structures in different parametric regimes. Finally, in Sec. V, we summarize our findings and present our conclusions.

II. MATHEMATICAL SETUP & QUALITATIVE THEORETICAL ANALYSIS

A. The basic model

As the basic mathematical model for our setup, we employ the widely recognized coupled Gross-Pitaevskii equations for two complex wave functions, $\psi_1(\mathbf{r}, t)$ (the vortical component), and $\psi_2(\mathbf{r}, t)$ (the bright component) [1–3]. For simplicity, equal masses $m_1 = m_2 = m$ of the species atoms are considered. Let an axisymmetric harmonic trap be character-

ized by a perpendicular frequency $\omega_\perp$ and by an anisotropy $\kappa = \omega_\parallel/\omega_\perp$. Using the trap units $\tau = 1/\omega_\perp$ for the time, $l_{\rm trap} = \sqrt{\hbar/(m\omega_\perp)}$ for the length, and $\varepsilon = \hbar\omega_\perp$ for the energy, the equations of motion are written in dimensionless form

$$i\dot{\psi}_1 = -\frac{1}{2}\nabla^2\psi_1 + \left[V(\mathbf{r}) + g_{11}|\psi_1|^2 + g_{12}|\psi_2|^2\right]\psi_1, \quad (1)$$

$$i\dot{\psi}_2 = -\frac{1}{2}\nabla^2\psi_2 + \left[V(\mathbf{r}) + g_{21}|\psi_1|^2 + g_{22}|\psi_2|^2\right]\psi_2, \quad (2)$$

where the overdot stands for the temporal partial derivative,

$$V(\mathbf{r}) = (x^2 + y^2 + \kappa^2 z^2)/2 \quad (3)$$

is the trap potential, while g_{ij} is a symmetric 2×2 matrix of nonlinear interactions. Physically, the interactions are determined by the scattering lengths a_{ij} [51]:

$$g_{ij}^{\rm phys} = 2\pi\hbar^2 a_{ij}(m_i^{-1} + m_j^{-1}), \qquad i,j = 1,2. \quad (4)$$

In this work, we consider the symmetric case $a_{11} = a_{22} = a > 0$, so the self-repulsion coefficients are equal to each other. It should be noted that while the setting, e.g., of ^{87}Rb features slight differences between the a_{ij}'s [52], it is possible to experimentally engineer the well-known, so-called Manakov case of equal interactions [53]. Without loss of generality, the relevant coefficients can be normalized to the unit value, $g_{11} = g_{22} = 1$. With this choice, the (conserved) numbers of trapped atoms are given by the relations

$$N_1 = \frac{l_{\rm trap}}{4\pi a}\int |\psi_1|^2 d^3\mathbf{r} = (l_{\rm trap}/a)n_1, \quad (5)$$

$$N_2 = \frac{l_{\rm trap}}{4\pi a}\int |\psi_2|^2 d^3\mathbf{r} = (l_{\rm trap}/a)n_2. \quad (6)$$

In real experiments the ratio $l_{\rm trap}/a$ ranges typically from a few hundreds to a few thousands. In what follows, n_1 and n_2 will be important control parameters. The cross-repulsion coefficient will be assumed as $g_{12} = 1 + g$, with a small positive parameter g. The condition $g > 0$ is required for the phase separation regime to take place [54, 55], as has also been experimentally manifested in [56].

Since we intend to consider soft excitations on a stationary background, two more parameters will be used as well, namely the chemical potentials μ_1 and μ_2. The numbers of particles n_1 and n_2 are dependent upon μ_1 and μ_2. We are mainly interested in the Thomas-Fermi (TF) regime $\mu_1 \gg 1$, when the (single component) background density profile is given by a simple approximate formula

$$|\psi_1^{(0)}|^2 = \rho(\mathbf{r}) \approx \mu_1 - V(\mathbf{r}). \quad (7)$$

The typical sizes of the trapped cloud are thus $R_\perp = \sqrt{2\mu_1}$ and $R_z = R_\perp/\kappa$, while a typical width of an empty vortex core is $\xi_* \sim 1/\sqrt{\mu_1}$. Importantly, a filled vortex core can have a width w which is essentially larger than ξ_*. Roughly w can be estimated as

$$w \sim n_2^{1/2}\mu_1^{-3/4}, \quad (8)$$

since an effective volume of the bright component is $\sim w^2\sqrt{\mu_1}$ (assuming a bright component that completely fills the vortex density dip; such a regime with $\mu_1 \approx \mu_2$ is typical for the critical phenomena under consideration; see Fig. 1 for example), while a typical density of the bright component is $\sim \mu_1$. The inequality $w > \xi_*$ can be the reason for instability of a certain kind, as we will see further.

However, it is relevant to keep in mind that the VRB solutions may exist for a wide range of μ_2 and not just for μ_2 comparable to μ_1. A good example to draw analogies with is the dark-bright solitons of [57] where the analytical solution makes it clear that roughly the solutions exist for a very broad range of $\mu_2 < \mu_1$.

B. Variational approach and approximate Hamiltonian

In the Thomas-Fermi regime, a typical time period for vortex motion is parametrically long, $\tau_{\rm vort} \sim \mu \gg 1$ (in terms of trap time units), since the quantum of circulation is $2\pi \sim R_\perp^2/\tau_{\rm vort}$. On the other hand, typical periods of potential oscillations (sound modes) are about 1 and shorter. Thus, the latter hard degrees of freedom are well separated from the soft degrees of freedom (associated with the vortex). As sound modes of our Hamiltonian system (1)-(2) are not excited (sitting at much higher frequencies in the TF limit), the dynamics of soft modes can be described self-consistently through an appropriate effective vortex Lagrangian [58]. Here we briefly discuss some basic properties of such a variational description.

To begin, let us seek to describe the long-scale slow dynamics of a closed vortex filament in a trapped single-component BEC. To that effect, we leverage two equations for the superfluid velocity field $\mathbf{v}(\mathbf{r},t)$. The first equation is the (truncated) continuity equation on the given density background,

$$(\nabla\cdot\rho\mathbf{v}) \approx 0. \quad (9)$$

This equation neglects the presence of a density dip in the vortex core. The second equation is for the vorticity $\mathbf{\Omega}(\mathbf{r},t) = \text{curl}\,\mathbf{v}$, which is singularly distributed along the vortex central line,

$$\mathbf{\Omega}(\mathbf{r},t) = \Gamma\oint \delta(\mathbf{r} - \mathbf{R}(\beta,t))\mathbf{R}_\beta d\beta, \quad (10)$$

where $\Gamma = 2\pi\hbar/m$ is the circulation quantum, $\delta(...)$ is the three-dimensional Dirac delta-function, and the unknown vector function $\mathbf{R}(\beta,t)$ describes the shape of the vortex in three dimensions, with β being an arbitrary longitudinal parameter along the line. The central line is assumed to move with a velocity determined by equations (9)-(10) but locally averaged over the vortex core cross-section. No effects of vortex core inertia are included into this approximate model.

It has been previously recognized that, in fact, the above inertia-free approximation corresponds to a variational dynamics for the vortex configuration [39, 58, 59] (see details in Appendix A). In particular, if the shape of the distorted vortex ring is given in the cylindrical coordinates by two real

functions $R(\varphi,t)$ and $Z(\varphi,t)$ characterizing the radial extent of the VR and its z-location, then the two scalar equations of motion are of the following non-canonical Hamiltonian form,

$$\Gamma\rho(R,Z)R\dot{Z} = \delta\mathcal{H}_v/\delta R, \quad (11)$$

$$-\Gamma\rho(R,Z)R\dot{R} = \delta\mathcal{H}_v/\delta Z. \quad (12)$$

Here the Hamiltonian functional $\mathcal{H}_v\{R(\varphi),Z(\varphi)\}$ is the energy associated with the presence of the vortex on the given density background. The right hand sides of the above equations are the corresponding variational derivatives. In such a description, distortions of the vortex ring are treated as waves in a spatially one-dimensional conservative system (with the periodic boundary conditions corresponding to the angular coordinate φ). The Hamiltonian approach is a well known and extensively deployed technique in the theory of nonlinear waves. Indeed, we employ it also in our present analysis.

In particular, linearized equations of motion for small deviations of the vortex ring take the form

$$\delta\dot{Z}_m \propto (B_m/\mu)\delta R_m, \qquad -\delta\dot{R}_m \propto (A_m/\mu)\delta Z_m, \quad (13)$$

where integer m is the wavenumber of the azimuthal Fourier mode. The real coefficients $A_m(\kappa,\mu)$ and $B_m(\kappa,\mu)$ are determined by the Hamiltonian. The squared eigenfrequencies are thus $\omega_m^2 \propto A_m B_m/\mu^2$, and they should be positive for linear stability.

Unfortunately, it is impossible to express the Hamiltonian explicitly because of technical difficulties (see Appendix A). However, one can use approximate Hamiltonian functionals to analyze basic properties of the vortex dynamics. In particular, the so called Local Induction Approximation (LIA) works in the deep Thomas-Fermi refime, when $\ln(\mu)\gg 1$, and it gives us approximate expressions for the coefficients A_m and B_m (see Appendix B).

Without an explicit Hamiltonian at hand, we are only able to extract just some general consequences of the variational description. However, three of them are crucially important and are briefly discussed below.

First off, going slightly beyond LIA (see the details in the Appendix B), we obtain an estimate for a stable interval of the anisotropy parameter where $A_m B_m > 0$ for all m [39, 49, 50],

$$1 \leqslant \kappa \leqslant \kappa_c(\mu) \approx 2 - \mathcal{O}(1/\ln(\mu)). \quad (14)$$

The second important point is that, according to the general theory of Hamiltonian systems, for the stable parametric interval (14), there exist so-called normal complex variables a_m (and their complex conjugate a_m^*) in our system,

$$\mathsf{a}_m \sim \frac{\sqrt{|A_m|}\delta R_m - \mathsf{i}\sqrt{|B_m|}\delta Z_m}{\sqrt{2|\omega_m|}}, \quad (15)$$

which are related to canonical action-angle variables S_m and Φ_m by formula $\mathsf{a}_m = \sqrt{S_m}\exp(\mathsf{i}\Phi_m)$. The quadratic part of the Hamiltonian acquires an especially simple form,

$$\mathcal{H}_v^{(2)} = \sum_{m=-\infty}^{+\infty} \omega_m \mathsf{a}_m^*\mathsf{a}_m, \quad (16)$$

and the equations of motion are

$$\mathsf{i}\dot{\mathsf{a}}_m = \partial\mathcal{H}_v/\partial\mathsf{a}_m^*. \quad (17)$$

Thus, in the linear approximation we have just a set of uncoupled harmonic oscillators. The dynamics of each oscillator is reduced to a rotation of the phase,

$$\mathsf{a}_m(t) \approx \mathsf{a}_m(0)\exp(-\mathsf{i}\omega_m t), \quad (18)$$

and all the wave actions S_m are conserved.

Nonlinear interactions between the oscillators are described by cubic and higher-order terms in the Hamiltonian expansion in powers of a_m. Most of them violate conservation of the wave action. In particular, the three-wave Hamiltonian is of the general form

$$\mathcal{H}_v^{(3)} = \frac{1}{6}\sum \delta_{m_1+m_2+m_3}[U_{m_1,m_2,m_3}\mathsf{a}_{m_1}^*\mathsf{a}_{m_2}^*\mathsf{a}_{m_3}^* + c.c.] + \frac{1}{2}\sum \delta_{m_1+m_2-m_3}[V_{m_1,m_2,m_3}\mathsf{a}_{m_1}^*\mathsf{a}_{m_2}^*\mathsf{a}_{m_3} + c.c.], \quad (19)$$

with some interaction coefficients U and V. Here δ denotes the discrete (Kronecker) delta. The terms $\mathsf{a}_{m_1}^*\mathsf{a}_{m_2}^*\mathsf{a}_{m_3}$ describe a nonlinear process where one wave decays into two waves, while the terms $\mathsf{a}_{m_1}\mathsf{a}_{m_2}\mathsf{a}_{m_3}^*$ correspond to the opposite process of fusion. Both decay and fusion are referred to as $1 \longleftrightarrow 2$ three-wave interactions. Analogously, interactions $\nu_1 \longleftrightarrow \nu_2$, with non-negative integers ν_1 and ν_2, for $(\nu_1+\nu_2) > 3$ are present as well. Which nonlinear process is the most important depends on many factors, in particular on the spectrum ω_m, because the resonance conditions for the process are

$$\sum_{\sigma=1}^{\nu_1} m_\sigma = \sum_{\sigma=\nu_1+1}^{\nu_1+\nu_2} m_\sigma, \qquad \sum_{\sigma=1}^{\nu_1}\omega_{m_\sigma} \approx \sum_{\sigma=\nu_1+1}^{\nu_1+\nu_2}\omega_{m_\sigma}. \quad (20)$$

We will see later that in our system a specific nonlinear instability may take place as the result of a $0 \longleftrightarrow 3$ interaction with a particular set of wavenumbers.

The third important observation is that within the stability interval the coefficients A_0, B_0, A_1, and B_1 are negative, while all the coefficients for $m \geqslant 2$ are positive. This fact implies that the values ω_0 and $\omega_1 = \omega_{-1}$ have the negative sign [39]. Physically this indicates the opposite direction of rotation for modes with $m = 0$ and $m = \pm 1$.

C. Linear $m = 2$ instability

Let us now consider a vortex ring with the core filled by the second component. The first instability encountered upon increasing anisotropy (past the spherical condensate limit) is the one associated with $m = 2$ and hence this is the one with which we start our considerations. We may assume that in some cases the role of the bright component is reduced mainly to increasing an effective relative width of the vortex core. In other words, a "fat", filled vortex ring can behave similarly to a vortex ring in a one-component system but with a smaller μ,

up to rescaling of the time variable. In such cases, the geometric regularization parameter becomes $w/R_* \sim n_2^{1/2}\mu_1^{-5/4}$ instead of $\xi_*/R_* \sim 1/\mu_1$, so the critical anisotropy value (corresponding to the $m = 2$ instability) changes to

$$\tilde{\kappa}_c(n_2, \mu_1) \approx 2 - \mathcal{O}(1/\ln[n_2^{-1/2}\mu_1^{5/4}]) < \kappa_c(\mu_1). \quad (21)$$

For a given μ_1 and a given anisotropy parameter within the region $\tilde{\kappa}_c(n_2, \mu_1) < \kappa < \kappa_c(\mu_1)$, the filled vortex ring is unstable despite the fact that the corresponding empty-core ring is stable. Apparently, there should exist a critical value $n_{2,c}(\kappa, \mu_1)$, such that $\tilde{\kappa}_c(n_{2,c}, \mu_1) = \kappa$. The vortex-ring-bright structure becomes unstable when $n_2 > n_{2,c}$. In our numerical computations, that will be reported below, we will indeed observe such an instability near the right side of the (empty-vortex stable) anisotropy interval $[1 : \kappa_c(\mu_1)]$. Hence, the presence of the second component narrows the interval of the anisotropy parameter κ, within the oblate condensate geometry, for which the VR is dynamically stable.

D. Nonlinear parametric instability

The negative value for ω_0 and positive value for ω_2 additionally render possible a nonlinear parametric resonance corresponding to explosive three-wave nonlinear interaction of $0 \longleftrightarrow 3$ type and described by terms as $[U\mathsf{a}_0^*\mathsf{a}_2^*\mathsf{a}_{-2}^* + c.c.]$ in the Hamiltonian expansion on powers of the normal complex variables. In Ref. [39], this phenomenon was considered for a single-component condensate (with a different density profile) within the simplified LIA approach. In the present work, it is numerically explored for binary condensates, within the fully three-dimensional model of the coupled Gross-Pitaevskii equations.

The condition for this nonlinear resonance is

$$2\omega_2 + \omega_0 \approx 0, \quad (22)$$

and it is satisfied near a definite value of the anisotropy $\kappa_{\rm prm}$, depending upon n_2 and μ_1. It should be noted here that $\kappa_{\rm prm}$ is sensitive to the logarithm of the effective ratio $w/R_* \sim n_2^{1/2}\mu_1^{-5/4}$. For comparison, in the empty-core case the solution is sensitive to the logarithm of $\xi_*/R_* \sim 1/\mu_1$. Interestingly, the logarithmic correction is so essential for condition (22) that even at quite large $\mu_1 \sim 40$ we cannot safely use the LIA prediction $\kappa_{\rm prm} = \sqrt{16/7}$ for the resonant value [39]. Thus, for a filled vortex ring in a binary condensate with realistic parameters, the LIA prediction yields practically inaccurate results. In general, as n_2 increases, $\kappa_{\rm prm}(n_2, \mu_1)$ decreases. An approximate, yet more detailed description of this instability is given in Appendix C. Nevertheless, we believe that the combination of the quantitative analysis for the case of the empty cores in the relevant Appendix, and the qualitative, numerically observed generalization for the case of the filled cores is sufficient to provide a reasonable physical understanding of the relevant phenomenology.

E. Linear $m = 1$ instability

Besides the $m = 2$ instability, which is qualitatively the same as in the single-component case, we have detected numerically a qualitatively different linear instability caused by the presence of the bright component. This instability involves 3D modes with azimuthal number $m = 1$, and it is particularly relevant in the middle of the parametric interval $1 < \kappa < \kappa_c(\mu_1)$. It is important to highlight that this is a distinct instability scenario than the $m = 1$ case occurring for $\kappa < 1$. Basically, the unstable mode is a mix of deviation of the vortex central line from the perfect axially symmetric circular (annular) shape and a nonuniform cross-section of the core along the vortex. For this new instability, we have not yet developed an accurate quantitative theoretical description. However, we believe that a proper qualitative explanation can be provided as follows.

The point is that the above described mechanism of instability for the $m = 2$ mode was based on the assumption that the filling component does not present its own dynamics. Such a regime is only possible if the corresponding degrees of freedom remain hard. However, the assumption is apparently incorrect if nonuniform longitudinal oscillations of the bright component along the vortex filament become essentially excited due to softening of their effective potential energy. Qualitatively, the longitudinal flows are similar to a one-dimensional gas dynamics with an effective "equation of state" where the "gas density" is proportional to the mass of the filling component per unit length of the vortex. The "equation of state" is however unusual since the "speed of sound" decreases as the "gas density" increases. The softening corresponds to an effective decrease in "speed of sound" at sufficiently large "gas density", and it is presumably similar to the mechanism of the "sausage" instability for a classical hollow columnar vortex due to the presence of surface tension [60]. In the case of binary BECs, the effective surface tension between the two components is roughly proportional to $\sqrt{g_{12} - 1} = \sqrt{g}$, while the width of a domain wall between the components is proportional to $1/\sqrt{g}$ [61]. Of course, the applicability of the analogy with the classical picture assumes that the wall is narrow in comparison with an effective vortex core radius. In our case, since we deal with small values of g, this assumption is not valid, so the analogy with a classical vortex is quite distant. Nevertheless, as it has been observed in a recent work [44] numerically, the softening of the longitudinal modes does take place as the amount of filling component is increased. In the trapped system, they couple with the $m = 1$ mode of ring shape oscillations and produce an oscillatory instability. Mathematically, this coupling can be expressed by a quadratic Hamiltonian of the following form,

$$H_{\rm cpl} = -\frac{1}{2}p^2 - \frac{\omega_1^2}{2}q^2 + \frac{1}{2}P^2 + \frac{\Omega_1^2}{2}Q^2 + \zeta qQ, \quad (23)$$

where canonical variables q and p represent the ring deviations (they are proportional to δR_1 and δZ_1, respectively), while Q and P represent the first Fourier harmonic of the longitudinal oscillations of the filling component. The corresponding function $\tilde{Q}(\varphi, t)$ ["gas density"] is proportional to the den-

sity integral of the second component over the cross-section $\arctan(y/x) = \varphi$ of the filled vortex. More precisely,

$$\tilde{Q}(\varphi, t) \propto \int |\psi_2(r, z, \varphi, t)|^2 r dr dz. \tag{24}$$

A canonically conjugate function $\tilde{P}(\varphi)$ is basically proportional to the potential of longitudinal velocity of the bright component.

The parameter ω_1^2 here is the squared frequency of $m = 1$ mode of transverse oscillations as determined by coefficients A_1 and B_1 with a given ratio w/R_*. The frequency of the longitudinal mode is denoted as Ω_1. It basically coincides with the longitudinal frequency of a straight filled vortex at wavelength $2\pi R_*$, for the same mean filling per unit length, and for periodic boundary conditions. There is also a coupling coefficient ζ between these two degrees of freedom (the only admissible by symmetry reasons, but actually unknown due to the absence of explicit expression for the Hamiltonian).

It is important that the two negative signs in expression (23) are in accordance with the opposite direction of rotation for the first mode of the ring shape deviations, while the longitudinal-flow degree of freedom, when taken separately, behaves as an ordinary oscillator with positively defined self-energy.

The eigenvalues of Hamiltonian (23) are

$$\lambda_{1,2}^2 = \frac{1}{2}\Big[-\omega_1^2 - \Omega_1^2 \pm \sqrt{\left(\Omega_1^2 - \omega_1^2\right)^2 - 4\zeta^2}\,\Big]. \tag{25}$$

It is clear from the above expression that with Ω_1 sufficiently close to $|\omega_1|$, the eigenvalues become complex, and an oscillatory instability takes place. It is interesting to note that with sufficiently small ζ the above formula predicts a finite unstable interval in Ω_1, so a re-stabilization may occur when the softening of the longitudinal mode is too deep (small Ω_1). This will be explored in our numerical computations below.

F. Massive-core transverse instability

Another important dynamical effect not covered by the Lagrangian (A1) is the transverse inertia of the vortex core. For two-dimensional flows, this effect has been considered in recent works [46, 47]. The three-dimensional case studied here is more complicated. In general, the local cross-section of a filled vortex core is not circular but rather elliptic or even more distorted, and therefore it is less straightforward to perform an exhaustive theoretical analysis for a "fat" distorted massive core. However, roughly we may take into account only the most important parameter, i.e., the transverse mass (see below). This is different from the longitudinal mass coinciding with the bright component mass per unit length of the vortex (the corresponding longitudinal flows have been briefly discussed in the previous subsection). Here we consider the effect of transverse mass upon stability of a filled vortex ring in a trap. The transverse mass $M_\perp$ (a local characteristic per unit length) includes (as a part) the mass of the bright component, but also the added mass of the vortex component caused by the density depletion. This added mass is qualitatively similar to the well-known added mass in classical hydrodynamics, since every transverse motion of the core is accompanied by an additional potential flow in the vortex component. That flow is effectively localized on the scale of the core width. Accordingly, an additional kinetic energy is associated with such flow. This kinetic energy is a quadratic functional in time derivatives of the vortex configuration. Therefore, it has to be added to the Lagrangian (A1). Together with the transverse kinetic energy of the bright component, we have the term

$$\mathcal{K}_\perp = \frac{1}{2}\oint M_\perp(\beta, t)|\mathbf{R}_{t,\perp}|^2 |\mathbf{R}_\beta| d\beta.$$

The above expression essentially contains the definition of the transverse mass. Unfortunately, it is very difficult to calculate the added mass analytically, but it is of the same order as the longitudinal mass of a non-weakly filled core. Therefore, as a simple estimate we may use the following formula,

$$M_\perp \sim M_\parallel \sim n_2/\sqrt{\mu_1}.$$

Linearized equations of motion for small deviations of the ring now are

$$-M_\perp R_* \ddot{R} + \Gamma\rho_* R_* \dot{Z} = \delta\mathcal{H}_v^{(2)}/\delta R, \tag{26}$$
$$-M_\perp R_* \ddot{Z} - \Gamma\rho_* R_* \dot{R} = \delta\mathcal{H}_v^{(2)}/\delta Z. \tag{27}$$

When written in Fourier representation, these equations take the simple form

$$-\frac{M_\perp}{\Gamma\rho_*}\ddot{R}_m + \dot{Z}_m = \frac{\Gamma}{4\pi R_*^2} A_m R_m, \tag{28}$$
$$-\frac{M_\perp}{\Gamma\rho_*}\ddot{Z}_m - \dot{R}_m = \frac{\Gamma}{4\pi R_*^2} B_m Z_m. \tag{29}$$

With a fixed mass, the mathematical structure of these equations is the same as for a particle in a constant magnetic field in the presence of an external quadratic potential. The eigenfrequencies for the above system are determined by a biquadratic equation,

$$(\tau\omega_m^2 - \hat{A}_m)(\tau\omega_m^2 - \hat{B}_m) = \omega_m^2, \tag{30}$$

where $\tau = M_\perp/(\Gamma\rho_*)$, while $\hat{A}_m = \Gamma/(4\pi R_*^2)A_m$ and $\hat{B}_m = \Gamma/(4\pi R_*^2)B_m$. It is easy to see that if $\hat{A}_m$ and $\hat{B}_m$ are both negative, as is the case for $m = 0$ and $m = 1$, then at sufficiently large values of τ the discriminant of the above equation becomes negative. This signals the appearance of an oscillatory instability.

For a "completely filled" VRB in the deep TF limit, we can roughly put $R_* = \sqrt{2\mu_1/3}$, $\rho_* = 2\mu_1/3$, $M_\perp = 4\pi n_2/(2\pi R_*)$, and

$$A_m = (m^2 - 3)\ln(C_{\rm fit}\mu_1^{5/4} n_2^{-1/2}),$$
$$B_m = (m^2 - \kappa^2)\ln(C_{\rm fit}\mu_1^{5/4} n_2^{-1/2}),$$

where $C_{\rm fit}$ is a fitting constant. Then, since $\Gamma = 2\pi$, we will have in Eq. (30): $\tau = n_2/[\pi(2\mu_1/3)^{3/2}]$, $\hat{A}_m = 3A_m/(4\mu_1)$,

$\hat{B}_m = 3B_m/(4\mu_1)$. With fixed parameters μ_1 and n_2, we can solve Eq. (30) for $\omega_m(\kappa)$ and compare them to the numerical results, similarly to Fig. 3 in the work [49] on VRs. To explore this potential instability for $m = 0$, as well as more generally the above analytical predictions, we will now turn to numerical computations.

III. COMPUTATIONAL SETUP

Our numerical computation includes identifying numerically exact VRB stationary states, characterizing their stability properties through the Bogolyubov-de Gennes (BdG) spectral analysis [3, 62], as well as exploring the VRB unstable dynamics. To find a stationary state, we apply the finite element method for a spatial discretization of the fields and subsequently utilize the Newton's method for convergence given a suitable initial guess; see the parametric continuation below for the numerical continuation of the VRB states from its underlying analytic linear limit. Since the states are rotationally symmetric about the z-axis, we have identified them in the reduced (ϱ, z) cross section, where $\varrho = \sqrt{x^2 + y^2}$. Upon convergence, the BdG spectrum of the state is collected using the partial-wave method [63–65], again in the (ρ, z) plane. In this work, we have collected the spectra of the pertinent low-lying angular Fourier modes $m = 0, 1, 2, ..., 5$ [64]. It is worth mentioning that this $2d$ reduced computation is far more efficient than a direct $3d$ computation, enabling us to investigate the VRB deep in the TF regime. Indeed, we have explored up to chemical potentials as large as $\mu_1 = 80$ for this three-dimensional structure in this work. Finally, when a genuinely $3d$ state is needed for dynamics, it is initialized from the $2d$ state using the cubic spline interpolation. Our dynamics is integrated using either the regular fourth-order Runge-Kutta method or a third-order operator splitting Fourier spectral method.

The VRB stationary states are parametrically continued from the underlying analytic linear limit at $(\mu_1 = 4, \mu_2 = 2)$ and $\kappa = 2$. In this setting, the two small-amplitude fields decouple. The VR state is a complex mixing of the degenerate states of the ring dark soliton $(|200\rangle + |020\rangle)/\sqrt{2}$ and the planar dark soliton $|001\rangle$ with a relative phase of $\pi/2$. The bright component is in the $|000\rangle$ ground state. Here, $|mnp\rangle$ represents a $3d$ quantum harmonic oscillator state in the Cartesian coordinates. These linear states are used as the initial guess for slightly larger chemical potentials (μ_1, μ_2) at fixed $\kappa = 2$. When a solution is found near the linear limit, it is then used as the initial guess for larger chemical potentials at $\kappa = 2$, and so on in this parametric continuation. By trial and error, we find that the following continuation path is both typical (the bright mass is neither too large nor small) and robust:

$$\mu_2 = \mu_1 - 1.2 - 0.8\exp(-0.5(\mu_1 - 4)). \tag{31}$$

In addition, when the chemical potentials are sufficiently large (i.e., $\mu_1 \gtrsim 10$), the existence of the VRB around this particular continuation path becomes robust and we can readily continue the states therein further in all other parameters, i.e., μ_2, κ, and g_{12}. For example, for a typical μ_1, μ_2 can be tuned in a wide parametric range. The lower bound increases with increasing μ_1 due to the tighter confinement of the vortex core and the upper bound is typically slightly below μ_1. Here, the bright mass in the stationary state is tuned by adjusting μ_2.

IV. NUMERICAL RESULTS

A. Stationary states and the BdG spectra

Several typical numerically exact VRB configurations are depicted in Fig. 2. In this work, we have continued the VRB state following the continuation path of Eq. (31) from the linear limit all the way to $\mu_1 = 80$ which is deep in the TF regime at $\kappa = 2$. Because the trap geometry is expected to have a strong influence on the VRB stability, we have explored the effect of $\kappa \in [0.5, 3]$ at three typical chemical potentials at $\mu_1 = 20, 40, 80$.

The BdG spectra of the VRB along these four continuation paths are summarized in Fig. 3. Overall, the gross structure is qualitatively very similar to that of the single-component VR [49]. The $m = 1$ mode becomes unstable exactly below $\kappa = 1$, i.e., for prolate condensates. It is important to clarify that this instability is an exponential one, associated with a purely real pair of eigenvalues. This is to be contrasted to the oscillatory instabilities associated with the $m = 1$ mode that are a genuine feature of the VRB structure (and absent for the VR one) for $\kappa > 1$ (see below). In the opposite direction, the $m = 2$ mode becomes unstable at $\kappa > 2$ (theoretically) and there is a finite chemical potential effect narrowing down the stability interval. The critical κ moves closer to the theoretical limit $\kappa = 2$ as μ_1 is increased. Then, there is a similar trend for the $m = 3$ mode, where the critical κ moves towards the theoretical limit of $\kappa = 3$ with an even stronger finite chemical potential effect. Between the two regimes, the VRB has a stable regime in the interval $1 < \kappa \lesssim 2$. Therefore, the VRB is most stable in a slightly oblate condensate.

The numerical spectra also compare favourably with the corresponding theoretical prediction of Eq. (30), shown in dashed gold and dashed black lines for the real and imaginary parts, respectively. In Eq. (30), there is a fitting parameter $C_{\rm fit}$, whose value is chosen to match the real part of the spectra, as motivated by the single-component VR work [49]. The $C_{\rm fit}$ is reasonably robust: our best fit at $\mu_1 = 20$ yields $C_{\rm fit} = 2.5$, the ones at $\mu_1 = 40$ and 80 are only slightly larger, yielding $C_{\rm fit} = 2.6$ in both cases. The increasing stable mode with increasing κ is the $m = 0$ mode, the modes of $m = 1, 2, 3$ can be readily identified due to their stability-instability transitions. Then, the yet higher-lying ones in increasing order correspond to $m = 4$ and 5, respectively. As μ_1 increases, it is noted that the numerical spectra move closer to the theoretical predictions. This parallels the corresponding findings in the single-component VR comparison [49], yet here we systematically generalize the results to the two-component VRB structure. Indeed, the latter is richer due to the modes associated with the presence of the second component. For example at $\mu_1 = 80$, the almost horizontal lines around $\mathrm{Im}(\lambda) = 0.15, 0.3, 0.45, 0.6, 0.75$ are due to $m = 1, 2, ..., 5$,

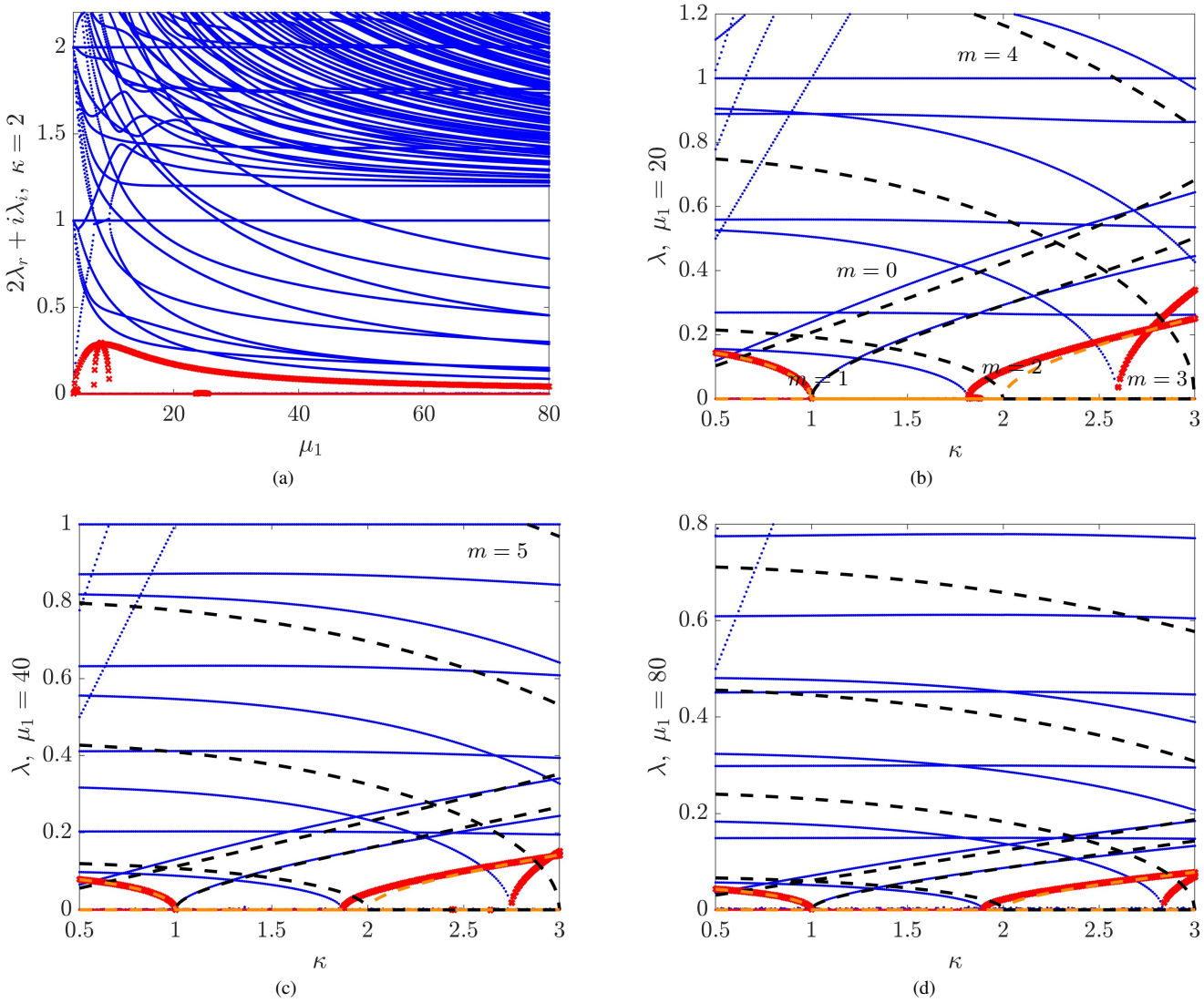

FIG. 3: In (a), the BdG spectra of VRBs are shown along the continuation path (of Eq. (31)) by varying μ_1 at fixed $\kappa = 2$. The real and imaginary parts of λ are shown as red crosses and blue dots, respectively (thus red pertains to instability). Here, the unstable real part is enlarged by a factor of 2 for clarity, and λ_r and λ_i are the real and imaginary parts of the eigenvalue λ, respectively. In (b-d), typical states in the TF regime are further continued in κ from the above path at fixed values $\mu_1 = 20, 40$ and 80, respectively. The gross feature is similar to that of the single-component VR, and the numerical spectra compare favourably with the analytical spectra (of Eq. (30)) shown as dashed gold (real part) and dashed black (imaginary part) lines. Here, it is easier to read the spectra by remembering that the mode m bifurcates at $\kappa = m$. Notice the improving nature of the analytical predictions as μ_1 increases. See the text for more details and an analogous comparison with the VR spectra in [49].

respectively. Such almost horizontal and nearly equidistant lines in Figs. 3(b)-3(d) correspond to the longitudinal modes. Mathematically, they are similar to sound modes in a 1D gas dynamics. In particular, the $m = 1$ longitudinal mode, together with the $m = 1$ transverse mode, produce the $m = 1$ instability at larger n_2, as we see in Fig. 4. The above longitudinal modes should not be mixed with modes $\lambda = \mathsf{i} = \mathsf{i}\omega_\perp$ and $\lambda = \mathsf{i}\kappa = \mathsf{i}\omega_\parallel$, which are characterized by strictly horizontal lines and correspond to the three independent types of oscillations of the whole configuration in the axisymmetric harmonic trap, in x, y, and z directions. These modes are "hard" in our terminology, while the longitudinal modes are rather "soft" with large values of the chemical potential μ_1.

B. Effect of the bright mass

To understand the effect of the filled bright mass, it is helpful to compare the spectra of the VRB and VR in detail. To this end, we compare their stability intervals and typical g rowth rates qualitatively using several representative observables as summarized in Table I. From these details, we iden-

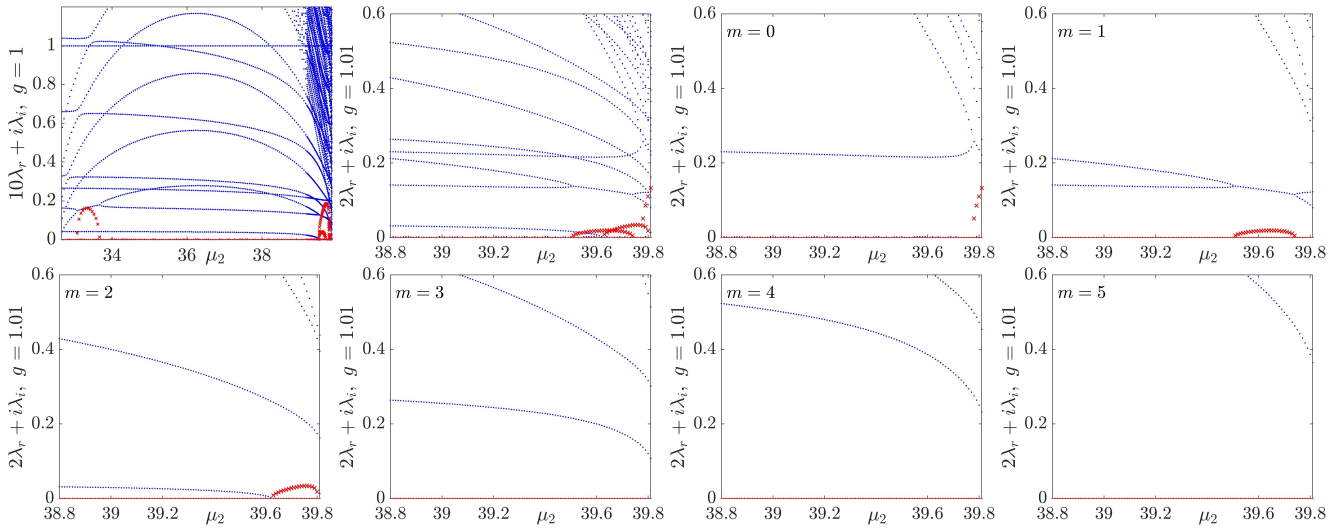

FIG. 4: The first panel showcasing the BdG spectrum as a function of μ_2 for a VRB illustrates the feature that μ_2 can be tuned in a wide range in the TF regime, spanning from a vanishing number of atoms to a system-size bright component. When the bright mass is varied, the VRB may suffer intervals of instability. The parameters are $\mu_1 = 40$, $32.65 < \mu_2 < 39.87$, $\kappa = 1.8$, $g_{12} = 1$. The second panel focuses on the relatively large μ_2 regime for another typical case $\mu_1 = 40$, $\kappa = 1.8$, but $g_{12} = 1.01$. Detailed inspection shows that the $m = 0, 1, 2$ modes can potentially become unstable as illustrated in the following panels depicting the spectra of the Fourier modes $m = 0, 1, ..., 5$, respectively. It should be noted that the $m = 1, 2$ instabilities are very common but the $m = 0$ instability is only restricted to large fillings if it exists and frequently occurs in a rather narrow parametric regime.

tify the following features:

1. The critical $\kappa_c = 1$ for the mode $m = 1$ appears to be exact for both the VRB and VR. For higher Kelvin modes (i.e., modes of higher m), the critical $\kappa_c(m) \lesssim m$ and approaches m as μ_1 increases. In addition, large chemical potentials tend to decrease the unstable growth rates for both states.

2. The stability interval systematically shrinks when the VR is filled with a bright component, i.e., the bright component tends to narrow down the stability regime.

3. Interestingly, when both the VRB and VR are unstable, the bright component tends to decrease the corresponding growth rates. In other words, while the presence of the bright component expands the region of instability, it concurrently weakens the instability growth rates in the cases where the instability was already present. However, this is not strictly satisfied, e.g., the bright component enhances $\lambda_r(m = 3, \kappa = 3)$ at small chemical potentials, and then lowers it at larger ones.

The narrowing of the stability interval by the bright mass suggests a stability-instability transition when μ_2 is tuned, at least for the $m \geq 2$ modes. This is indeed observed as we shall discuss below. However, it is interesting that we find the $m = 0$ and $m = 1$ modes can also have such transitions in this scenario. In addition, these instabilities are unprecedented in the VR context, to our knowledge, as the eigenvalues are complex ones. By contrast, the eigenvalue of the unstable $m = 1$ mode below $\kappa = 1$ is purely real. Our dynamic simulations confirm that the instabilities are indeed distinct ones, i.e., they appear to be genuinely caused by the interplay between the VR and the bright core and therefore they are not present in the single-component VR.

TABLE I: Some observables comparing the spectra of the VRB in Fig. 3 and the corresponding ones of VR [49]. Here, μ_1 for the VR is understood as its chemical potential, and $\lambda_r = \mathrm{Re}(\lambda)$.

States	observables	$\mu_1 = 20$	$\mu_1 = 40$	$\mu_1 = 80$
VR	$\kappa_c(m = 1)$	1	1	1
VR	$\kappa_c(m = 2)$	1.86	1.9	1.92
VR	$\kappa_c(m = 3)$	2.755	2.845	2.89
VR	$\lambda_r(m = 1, \kappa = 0.5)$	0.1572	0.09331	0.05435
VR	$\lambda_r(m = 2, \kappa = 2)$	0.08632	0.04619	0.02445
VR	$\lambda_r(m = 3, \kappa = 3)$	0.2931	0.1426	0.07254
VRB	$\kappa_c(m = 1)$	1	1	1
VRB	$\kappa_c(m = 2)$	1.815	1.87	1.895
VRB	$\kappa_c(m = 3)$	2.595	2.75	2.83
VRB	$\lambda_r(m = 1, \kappa = 0.5)$	0.1434	0.07857	0.04306
VRB	$\lambda_r(m = 2, \kappa = 2)$	0.08574	0.04279	0.02149
VRB	$\lambda_r(m = 3, \kappa = 3)$	0.3391	0.1518	0.06821

We have conducted a systematic study of the VRB spectra by tuning μ_2 at various values of κ and g_{12}. The first panel of Fig. 4 illustrates a Manakov case, and μ_2 is studied in its full range at $\mu_1 = 40$ and $\kappa = 1.8$. This is achieved by starting from the state at $(\mu_1, \mu_2) = (40, 38.8)$ and $\kappa = 1.8$ in Fig. 3, and then tuning μ_2 by either increasing or decreasing its value until the state no longer exists. As such, we find

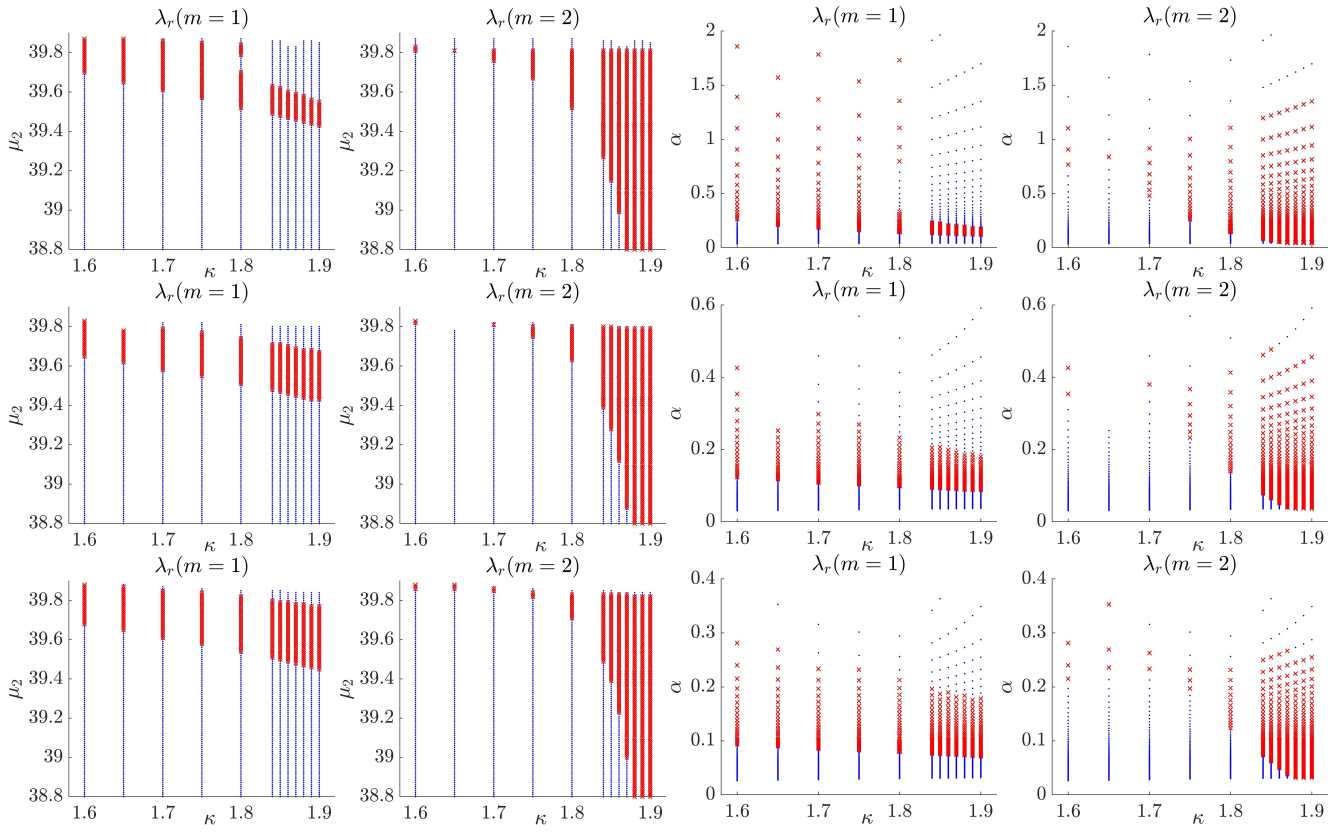

FIG. 5: The effect of the bright mass on the VRB stability for various κ and g_{12} values. The rows in turn are for $g_{12} = 1$, 1.01, and 1.02. Here, the blue points are for stable regimes and the red crosses are for unstable regimes. The maximum growth rate in an unstable interval is typically on the order of $O(0.01)$. The first and second column represent, respectively, for the $m = 1$ and $m = 2$ azimuthal modes, the stable (blue) and unstable (red) intervals in the plane of the chemical potential of the second species μ_2 vs. the anisotropy parameter κ, while the third and fourth column present the same information in terms of the two-component mass ratio α and the anisotropy parameter κ.

TABLE II: Some critical α and μ_2 values when the bright mass is tuned at different g_{12}. Here, $\kappa = 1.8$ and $\mu_1 = 40$.

g_{12}	$\alpha_c(m=1)$	$\alpha_c(m=2)$	$\mu_{2c}(m=1)$	$\mu_{2c}(m=2)$
1	0.1440	0.1440	39.52	39.52
1.01	0.0958	0.1345	39.5	39.62
1.02	0.0774	0.1238	39.53	39.71
1.03	0.0669	0.1158	39.58	39.8
1.04	0.0588	0.1061	39.63	39.88

that the VRB exists for this particular case in a wide interval $32.65 < \mu_2 < 39.87$, ranging from a faint bright soliton to a very fat core and also showing the robustness of the existence of the VRB structure at large μ_1. The spectrum reveals an interesting feature that the bright component can introduce unstable intervals, and both the $m = 1$ and $m = 2$ modes can become unstable.

To gain more intuition about the impact of the bright component mass, we introduce the mass ratio observable:

$$\alpha = N_2/N_1 \tag{32}$$

complementing the more abstract μ_2. Detailed inspection shows that the left instability (the one below $\mu_2 = 34$) is due to the mode $m = 1$, but the mass ratio there is extremely small $\alpha \in [0.0004247, 0.001128]$. On the other hand, both $m = 1$ and $m = 2$ modes become unstable when the filling is reasonably large $\alpha \gtrsim 0.1440$. The $m = 1$ instability in the two intervals is oscillatory in nature, therefore differs from the $m = 1$ instability in Fig. 3. By contrast, the $m = 2$ instability is real and appears to be a regular one.

The instabilities in the relatively large α regime appear to be common for a wide range of g_{12} and κ, and a typical spectrum at $g_{12} = 1.01$ and $\kappa = 1.8$ is also shown in Fig. 4. In addition to the total spectrum of the VRB coherent structure, we also show individual panels for the different azimuthal modes m and it is evident that the last panel of the first row and the first of the second row feature parametric intervals associated with instabilities. For instance this is not the case for the remaining panels of the second row of the figure, pertaining to $m = 3$, $m = 4$ and $m = 5$. While the $m = 1$ and $m = 2$ modes become unstable simultaneously in the Manakov case, this appears to be an interesting coincidence and in general they do not bifurcate together at other g_{12} and κ values. Furthermore, an unstable $m = 0$ mode is found despite the fact

that it only occurs in the highly filled regime. However, it should be noted that the unstable interval thereof can be much narrower in other parametric regimes of g_{12} and κ.

The critical α and μ_2 of the modes with $m = 1$ and $m = 2$ for a few g_{12} values are summarized in Table II, and we shall explore the effect of κ in the next subsection. As g_{12} increases, the critical α decreases for both modes, and the $m = 1$ mode bifurcates earlier than the $m = 2$ mode at a smaller mass ratio. The decreasing of α here is reasonable, as the inter-component repulsion becomes stronger, it presumably does not take much bright mass to produce the same effective strength of interaction for the induced instabilities.

C. Effect of κ on the critical transitions

Here, we investigate the κ-dependence of the bright-induced instability in the large α regime. The examples shown in the previous subsection suggest that the critical transitions clearly depend on κ. To this end, we compute the spectra with respect to μ_2 for a series of κ values by further increasing μ_2 to its upper limit from the appropriate states in Fig. 3. The results are illustrated in Fig. 5 and some typical numbers for the Manakov case are summarized in Table III.

Since Fig. 3 shows that the $m = 2$ instability is already present at $\kappa = 1.87$ before μ_2 is increased, this suggests that the critical chemical potential thereof should decrease when κ is increased. This is found to be essentially the case numerically in Fig. 4 for both the $m = 1$ and $m = 2$ modes. However, the effect of κ on the $m = 2$ mode is stronger: note that the critical mass has a much larger slope for the $m = 2$ mode. This produces an interesting exchange of bifurcation order as α increases. For example, this exchange happens around $\kappa = 1.8$ for the Manakov case; see Table III for details. In the regime $\kappa > 1.8$ the $m = 2$ instability bifurcates first, and in the regime $\kappa < 1.8$ the $m = 1$ instability bifurcates earlier instead.

While the lower critical point decreases for both the $m = 1$ and $m = 2$ modes, the upper critical point has different behaviours. We observe that the relevant instability intervals are gradually shifted to lower values of μ_2 as κ is increased for $m = 1$, while the respective intervals substantially widen for larger values of κ for the case of $m = 2$ but the upper critical point does not shift downward as that of $m = 1$. In the context of the mass ratio α, we observe a shrinking of the unstable intervals as κ is increased from 1.6 to 1.9 for the $m = 1$ mode, while the relevant intervals, on the contrary, expand (indeed, considerably near $\kappa = 1.9$, in the case of the $m = 2$ mode. Figure 5 also illustrates a systematic reduction of the critical α for all values of κ as g_{12} is increased. The decrease of the lower critical α is in line with Table II.

It is interesting that restabilization can occur when α is increased further, in line with the theoretical expectation, and more than one unstable intervals can also exist. While increasing g_{12} has an effect of lowering the critical α, the general features remain largely similar to those of the Manakov case. It is worth mentioning that these instabilities are, however, quite weak and a typical maximum growth rate in an unstable interval is only approximately $O(0.01)$. In line with our theoretical expectation, no unstable modes for $m \geq 3$ are found in these wide parametric regimes.

TABLE III: Some critical α and μ_2 values with respect to κ when the bright mass is tuned for the typical Manakov case in Fig. 5. The ones marked with a star (*) have rather narrow instability intervals. The "peculiar" trend of $\alpha_c(m = 2)$ at $\kappa \lesssim 1.65$ is because in this regime, μ_{2c} essentially saturates, the drop of α at $\kappa = 1.6$ is therefore dominated by the larger background size.

κ	$\alpha_c(m=1)$	$\alpha_c(m=2)$	$\mu_{2c}(m=1)$	$\mu_{2c}(m=2)$
1.60	0.2651	0.7675*	39.70	39.81
1.65	0.2112	0.8379*	39.65	39.81
1.70	0.1842	0.4370	39.61	39.75
1.75	0.1583	0.2606	39.56	39.67
1.80	0.1440	0.1440	39.52	39.52
1.84	0.1315	0.0789	39.48	39.26
1.85	0.1288	0.0658	39.47	39.15
1.86	0.1262	0.0525	39.46	38.99
1.87	0.1237	<0.042	39.45	<38.8
1.88	0.1213	<0.042	39.44	<38.8
1.89	0.1191	<0.043	39.43	<38.8
1.90	0.1169	<0.043	39.42	<38.8

D. Dynamical Simulations

We have conducted several typical dynamical simulations following the spectra. The unstable modes in Fig. 3 are similar to those of the single-component VR. For example, we have run three VRB dynamics with random perturbations at $\mu_1 = 20$ and $\kappa = 0.9, 2, 3$, where the dominant unstable modes are $m = 1, 2, 3$, respectively. In preparing the initial state, we perturb the stationary state with random noise of 5% in norm, and then the state is renormalized such that its norm remains unchanged. First, it is worth mentioning that the bright mass essentially follows the VR core. At $\kappa = 0.9$, the VRB tends to flip and meanwhile it also extends one of its ends towards the edge of the condensate. The VRB breaks into two pieces before almost making a full flip. At $\kappa = 2$, the VRB breaks into two parallel vortex-line-bright (VLB) filaments extending outside the BEC. Then, the two VLBs can contract and reconnect into a full VRB. The VRB can repeat this process multiple times, with the two VLBs oriented towards different directions, before finally getting highly excited and disordered into vortical filaments. The instability at $\kappa = 3$ is triggered much faster, and the VRB is broken into three VLBs following the $m = 3$ mode as expected. Because these dynamics are similar to the VR counterparts, we shall not discuss them further here.

As mentioned earlier, we have also identified two unstable modes that are not available to the single-component VR, the oscillatorily unstable $m = 1$ and $m = 0$ modes. The former is very common but the latter is restricted to rather narrow chemical potential intervals of a large bright mass. We now

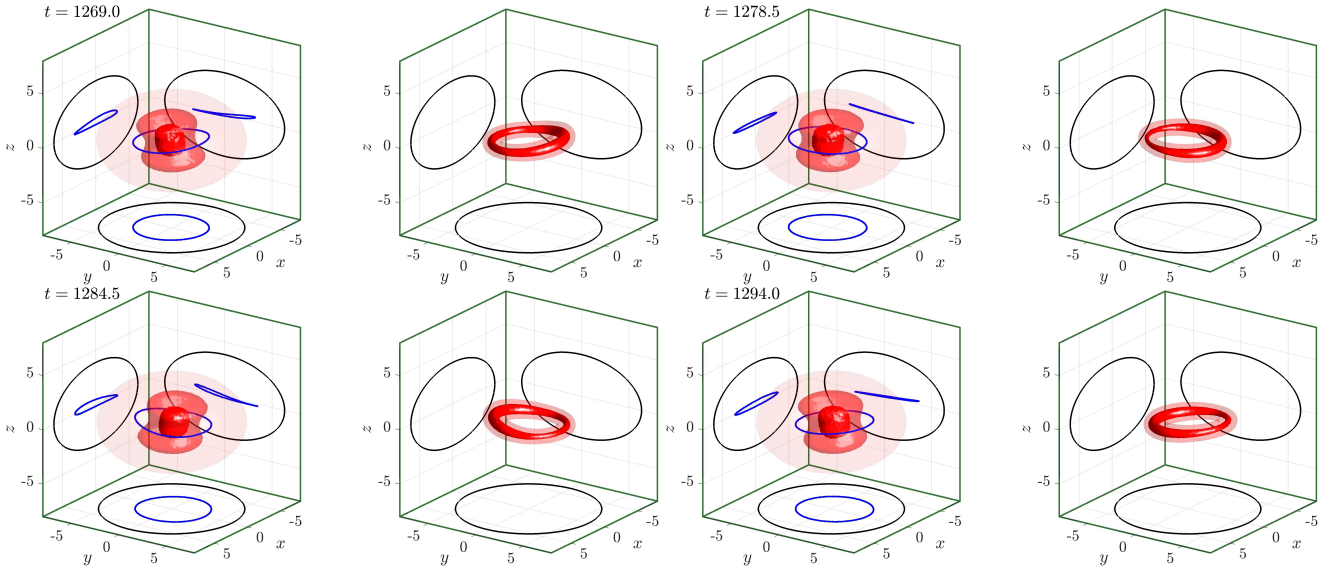

FIG. 6: Snapshots from the oscillatorily unstable evolution of an $m = 1$ mode after a long initial transient stage. For every given time, the left panel shows the component bearing the vortex ring, and the right panel shows the bright component, similarly to the top row of Fig. 1. In the oscillatory $m = 1$ unstable mode, the VRB first tilts and then propagates off the center, here in the approximately -y direction at $t = 1269$. The VRB then reaches the edge of the cloud and reverses its tilting direction. The VRB finishes the reversing at $t = 1278.5$ and propagates in the opposite direction, passing through the center at approximately $t = 1284.5$, and reaching the opposite end of the cloud. It similarly finishes reversing its tilting direction at $t = 1294$ and then runs back to the trap center. The VRB reaches the trap center at $t = 1300$, in a state similar to the one we started with at $t = 1269$, and then continues the cycle. The oscillation amplitude, however, gradually increases and the VRB eventually breaks into VLB filaments; see the full movie for details [66]. The simulation parameters are $\mu_1 = 20, \mu_2 = 19.4, \kappa = 1.65, \alpha = 0.2596, \lambda_r = 0.006895$, and the $m = 1$ mode is the only unstable mode.

discuss these two modes in detail.

The $m = 1$ oscillatorily unstable mode is illustrated in Fig. 6. The simulation illustrates the relevant unstable dynamics of the VRB structure after a long initial transient, focusing on its evolution past $t = 1269$. It might be appropriate to call it the VRB sloshing mode, as the VRB sloshes back and forth in the condensate. The VRB first tilts in the condensate and then propagates off the center, here in the approximately $-y$ direction at $t = 1269$. The VRB then collides with the edge of the cloud and reverses its tilting direction. The VRB finishes the reversal at $t = 1278.5$ and propagates in the opposite direction, passing through the center at approximately $t = 1284.5$, colliding with the trap again on the other side and similarly finishes reversing its tilting direction at $t = 1294$ and then runs back to the trap center. The VRB reaches the trap center at $t = 1300$, in a state similar to the one we started with, and then continues this cycle. The oscillation amplitude, however, increases and the VRB eventually breaks into VLB filaments; see the full movie for details [66]. The simulation parameters are $\mu_1 = 20, \mu_2 = 19.4, \kappa = 1.65, \alpha = 0.2596, \lambda_r = 0.006895$, and the $m = 1$ mode is the only unstable mode.

The $m = 0$ oscillatorily unstable mode is simpler to describe: this is the regular precessional mode of $m = 0$ around its equilibrium state but with a growing amplitude. As the amplitude grows, Kelvin modes are naturally excited, leading to instabilities. Since the mode is relatively familiar, we shall not discuss it in further detail here, but a full movie thereof is available [67]. In this case, the $m = 3$ mode is excited, and it is noticed that the VRB can break and reform for many cycles before the VRB is finally ejected out of the condensate. It is not very straightforward to find a parameter regime where $m = 0$ is the only unstable mode, but it is possible to find a suitable regime where it dominates. For the state in the movie, $\mu_1 = 20, \mu_2 = 19.61, \kappa = 1.7, \alpha = 0.8306, \lambda_r(m = 0) = 0.02388, \lambda_r(m = 1) = 0.008185, \lambda_r(m = 2) = 0.006596$. Note that the bright mass is very large, with a remarkable filling fraction as large as 83 percent.

E. Nonlinear Parametric Instability

So far we have explored the linear instabilities of the VRB structure. Now, we turn to the nonlinear parametric instability analyzed qualitatively in Sec. II D. Some numerical examples showcasing this instability are shown in Figs. 7 and 8. In Fig. 7 we show the vortex core locations by means of red points. Their projected positions are shown on each plane. In addition to the projected cores, we show the BEC density as thin contours at 0.2, 0.4, 0.6 and 0.8 of the maximum density. The BEC is started with the ring at 0.92 R_* with a small amount of $m = 2$ perturbation. After a long time, in this case about 1640 trap units of time, the $m = 2$ mode grows and becomes unstable. The vortex ring stretches until the ring is broken by part of the ring leaving the BEC. This can be seen in Fig. 7(c) and (d). Notice that while the results here are shown

for the case of a single-component VR, similar features arise in the case of the VRB.

Mode analysis, associated with this instability, is performed by extracting the core positions. These are sorted to be in azimuthal order. Then, analysis on the displacement and shape of the vortex ring was done assuming the following form for the vortex ring:

$$r(\varphi) = r_0 + \sum_m r_m e^{im\varphi}, \quad z(\varphi) = z_0 + \sum_m z_m e^{im\varphi}. \quad (33)$$

Here r, φ, and z are the cylindrical projections of $\mathbf{R}$. We have taken the real part of z_m and the real and positive part of r_m. These have been plotted in Fig. 8. Here, the nonlinear parametric instability can be identified as occurring around $\kappa = 1.25$. For$\kappa = 1.27$, i.e., some distance parametrically away from this instability, the ring is stable. As κ approaches the relevant parametric resonance point (from above) at $\kappa = 1.255$, it is noted that the ring tends to become unstable but the instability can decay and thereby a stable ring is restored. Another revival was observed until the instability amplifies and eventually the ring breaks. At the resonance of $\kappa = 1.25$, the ring becomes unstable quickly. In other simulations, for example with $\kappa = 1.14$, $n_2 = 78.5$, and $n_1 = 1570$, we observed similar behavior.

The parametric instability might be (partially) responsible for why the VR decays along some modes that are predicted to be linearly stable from the BdG spectrum [49]. It is therefore highly interesting to explore this type of resonance more systematically in the future, as it concerns a system that is *linearly stable but nonlinearly unstable*.

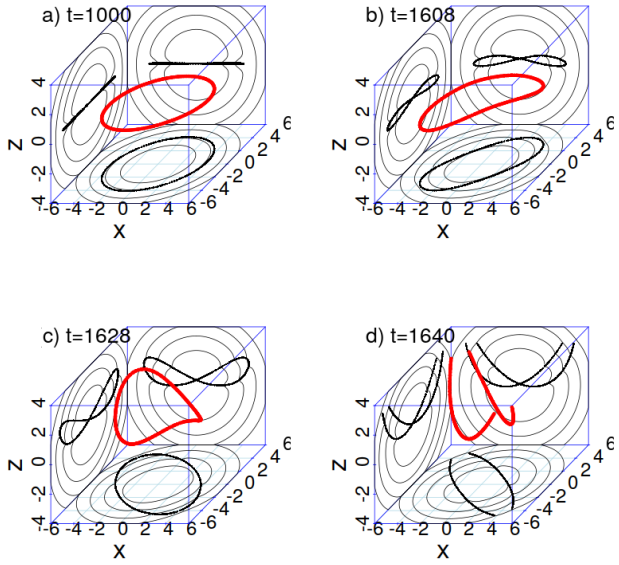

FIG. 7: Snapshots of a vortex ring are shown for a parametric instability. The positions of the extracted vortex cores are shown as red points and their projections are shown on each plane along with the density contours of the BEC. In this example, we have picked $\mu = 30$ with $\kappa = 1.25$. A small displacement from a circular structure was initially induced with an $m = 2$ mode in the radial direction.

V. CONCLUSIONS AND FUTURE CHALLENGES

The properties of the VRB show significant similarities with the single VR, but also nontrivial differences. The bright component has an effect towards slowing down the unstable dynamics, i.e., decreasing the instability growth rate when the structure is (already at the single-component VR level) unstable. Nevertheless, at the same time, the presence of the second (bright, filling) component also typically narrows the stability regime in the parameter space, especially as concerns the higher wavenumber instabilities, such as $m = 2$, $m = 3$ and so on. Perhaps more importantly, the latter component can endow the structure with additional instabilities in a regime where the VR would be structurally stable. These instabilities may be weak, yet they are of interest given their diverse possible origin, both in terms of the mode responsible and the linear vs. nonlinear nature of the instability. For instance, we discussed herein (and qualitatively justified) the oscillatory instability arising from the $m = 1$ mode, as well as the rather narrow instability of the $m = 0$ mode at the linear (spectral) level. There are also nonlinear, parametric instabilities that are present, arising from the resonance of modes such as $m = 0$ and $m = 2$, as we have also elucidated.

Naturally, there are numerous future directions that are emerging as a result of the present work. One important aspect of consideration of such topologically charged states is the consideration of not only density-induced (spin-independent) effects as is the case herein, but also of spin-dependent ones that arise in $F = 1$ and $F = 2$ spinor condensates [16, 17]. Hence, extensions of considerations to similar (but also Skyrmion) structures in 3-component BECs and beyond constitute a natural extension of the present work. Additionally, the recent exploration of advanced numerical methods, such as deflation [68] has enabled the characterization of far more elaborate topological structures in single-component, three-dimensional condensates. It would be of particular interest to examine generalizations of such states in multi-component settings and to examine their associated mechanisms of instability. Lastly, and similarly to the extensions of a single VR to multiple ones in single-component BECs [37], the interaction of a VRB with a VR or with another VRB would be interesting to quantify from an analytical and numerical perspective. Such studies will be reported in future publications.

Acknowledgments

W.W. acknowledges supports from the National Science Foundation of China under Grant No. 12004268, the Fundamental Research Funds for the Central Universities, China, and the Science Speciality Program of Sichuan University under Grant No. 2020SCUNL210. The work of V.P.R. was supported by the Russian Federation Program No. 0029-2019-0003. This material is based upon work supported by

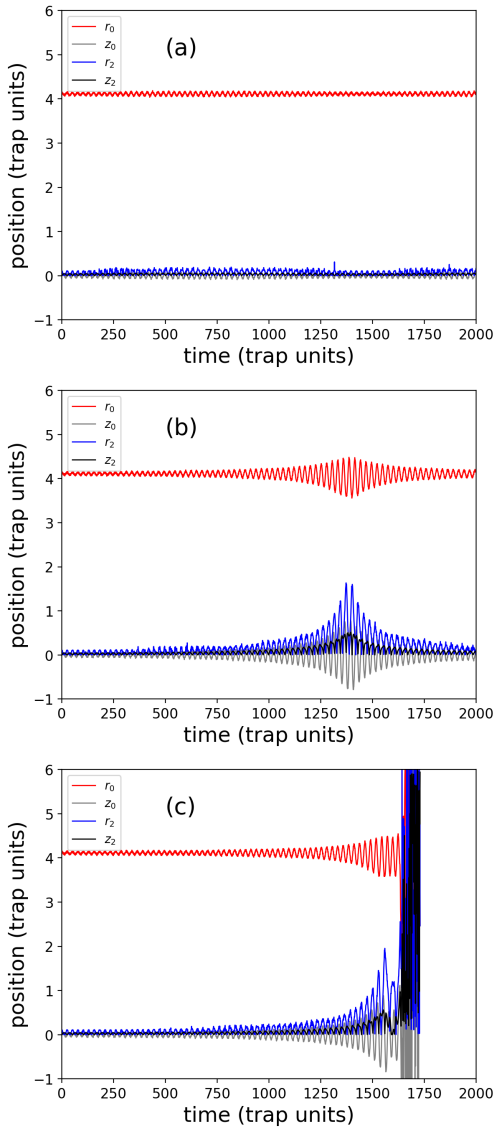

FIG. 8: Several examples of the extracted modes associated with the vortex core positions (see Eq. (33)) are shown for different geometries: (a) $\kappa = 1.27$, (b) $\kappa = 1.255$, and (c) $\kappa = 1.25$. The extracted vortex ring mode amplitudes shown are r_0 (red), r_2 (blue), z_0 (grey), and z_2 (black). In (a) a typical stable configuration with a seeded $m = 2$ perturbation is shown. In (b) a configuration near the maximal response associated with the parametric instability has a growth and decay of a mode of the vortex ring. Another revival was observed (for longer times, not shown here) without the ring being broken. In (c) at the point of resonance, the ring breaks after being unstable at a time of around 1640 trap units. All simulations are for a single-component BEC with $\mu = 30$.

the US National Science Foundation under Grant No. PHY-2110030 (P.G.K.). C.T. was supported by the US Department of Energy through the Los Alamos National Laboratory. Los Alamos National Laboratory is operated by Triad National Security, LLC, for the National Nuclear Security Administration of U.S. Department of Energy (Contract No. 89233218NCA000001). We thank the Emei cluster at Sichuan university for providing HPC resources.

Appendix A: The general form of vortex Lagrangian

The inertia-free approximation determined by Eqs.(9)-(10) corresponds to a Lagrangian functional of the general form [39, 58, 59]

$$\mathcal{L} = \Gamma \oint \mathbf{F}(\mathbf{R}) \cdot [\mathbf{R}_\beta \times \mathbf{R}_t] d\beta - \mathcal{H}_v\{\mathbf{R}(\beta, t)\}, \quad \text{(A1)}$$

with the Hamiltonian $\mathcal{H}_v$ being the vortex energy on the given density background. It is a non-local functional [59],

$$\mathcal{H}_v = \frac{1}{2} \oint \oint G_{kl}(\mathbf{R}_1, \mathbf{R}_2) R'_k(\beta_1) R'_l(\beta_2) d\beta_1 d\beta_2, \quad \text{(A2)}$$

where $G_{kl}(\mathbf{R}_1, \mathbf{R}_2)$ is the (appropriately regularized) matrix Green function for the auxiliary equation

$$\mathrm{curl} \frac{1}{\rho(\mathbf{r})} \mathrm{curl} \mathbf{A}(\mathbf{r}, t) = \mathbf{\Omega}(\mathbf{r}, t). \quad \text{(A3)}$$

Here $\mathbf{A}(\mathbf{r}, t)$ is a vector potential for the condensate flow around the vortex (it follows from Eq.(9) that $\rho \mathbf{v} \approx \mathrm{curl}\mathbf{A}$).

Unfortunately, it is impossible to solve equation (A3) analytically with the density profile $\rho(\mathbf{r}) = \mu - (x^2 + y^2 + \kappa^2 z^2)/2$ and thus express the Hamiltonian explicitly (the only known analytical solution corresponds to the Gaussian density profile and is expressed through a complicated integral [69]).

For self-consistency, the vector function $\mathbf{F}(\mathbf{R})$ should satisfy the condition [39, 58]

$$\mathrm{div}_{\mathbf{R}} \mathbf{F}(\mathbf{R}) = \rho(\mathbf{R}). \quad \text{(A4)}$$

The equation of motion in the vector form reads

$$\Gamma [\mathbf{R}_\beta \times \mathbf{R}_t] \rho(\mathbf{R}) = \delta \mathcal{H}_v / \delta \mathbf{R}, \quad \text{(A5)}$$

where $\delta \mathcal{H}_v / \delta \mathbf{R}$ is the variational derivative.

The above general equation takes different forms in different curvilinear coordinate systems. In particular, for description of a distorted vortex ring, we use the polar coordinates $\mathbf{R} = (R\cos\varphi, R\sin\varphi, Z)$, and we take the azimuthal angle φ as the longitudinal parameter β. The shape of the vortex is then given by two real functions $R(\varphi, t)$ and $Z(\varphi, t)$. For such configurations, the vector equation (A5) is equivalent to the pair of scalar equations of motion (11)-(12).

Appendix B: The spectrum within LIA and relevant extensions

For configurations such as a moderately perturbed vortex ring, the vortex Hamiltonian $\mathcal{H}_v$ is often taken in the LIA form, which corresponds to the deep TF regime [58]:

$$\begin{aligned} \mathcal{H}_v \approx \mathcal{H}_{\mathrm{LIA}} &= \frac{\Gamma^2}{4\pi} \Lambda \oint \rho(\mathbf{R}) |\mathbf{R}_\beta| d\beta \\ &= \frac{\Gamma^2}{4\pi} \Lambda \int \rho(R, Z) \sqrt{R^2 + R'^2 + Z'^2} d\varphi, \end{aligned} \quad \text{(B1)}$$

where $\Lambda = \ln(R_*/\xi_*) \approx \ln(\mu)$ is a large LIA constant, with R_* being the equilibrium ring radius. It is easily derived from expression (B1) that in the LIA framework $R_* = R_\perp/\sqrt{3}$. When small deviations $\delta R(\varphi, t)$ and $\delta Z(\varphi, t)$ are considered, the second-order Hamiltonian is

$$\mathcal{H}^{(2)}_{\rm LIA} \propto \ln(\mu) \sum_m \Big[(m^2-3)|\delta R_m|^2 + (m^2-\kappa^2)|\delta Z_m|^2\Big]. \tag{B2}$$

It is this second-order contribution that leads to the linearized motion of the VR in accordance with Eqs. (11-12). This yields the corresponding eigenfrequencies of VR motion as [39, 50]

$$\omega_m^{\rm LIA} \propto \frac{\ln(\mu)}{\mu}\sqrt{(m^2-3)(m^2-\kappa^2)}. \tag{B3}$$

Accordingly, the ring is stable in the parametric interval $1 \leqslant \kappa \leqslant 2$. The left edge of the stability interval is determined by the coefficient in front of $|\delta Z_1|^2$, while the right edge is determined by the coefficient in front of $|\delta Z_2|^2$. This result is valid in the limit $\mu \to \infty$. As to finite values of μ, the stability interval has been numerically found as $1 \leqslant \kappa \leqslant \kappa_c(\mu) < 2$ [49]. It is important for our present work that the critical value of the anisotropy parameter $\kappa_c(\mu)$ increases together with μ, tending to its asymptotic limit provided by Eq. (B3). To interpret this fact properly, we should recall that the LIA Hamiltonian (B1) is a limiting case of the more accurate non-local Hamiltonian functional (A2), with a regularized Green function. It is evident that a small non-dimensional geometric regularization parameter is $\xi_*/R_* \sim 1/\mu$. The corresponding second-order Hamiltonian for small deviations of the vortex ring should take the form

$$\mathcal{H}^{(2)}_v \propto \sum_m \Big[A_m(\kappa,\mu)|\delta R_m|^2 + B_m(\kappa,\mu)|\delta Z_m|^2\Big], \tag{B4}$$

with real coefficients $A_m = A_{-m}$ and $B_m = B_{-m}$. At large values $\mu \gg 1$, these functions behave as

$$A_m(\kappa,\mu) \approx \tilde{A}_m(\kappa) + (m^2-3)\ln(\mu), \tag{B5}$$

$$B_m(\kappa,\mu) \approx \tilde{B}_m(\kappa) + (m^2-\kappa^2)\ln(\mu), \tag{B6}$$

where $\tilde{A}_m$ and $\tilde{B}_m$ are finite regular functions corresponding to essentially non-local parts of the interactions. For linear stability, the product $A_m B_m$ should be positive. Due to general symmetry reasons, the coefficient $B_1(\kappa,\mu)$ takes zero value at $\kappa = 1$ for all μ, so the left edge of the stable interval does not change and involves the tumbling VR instability due to $m = 1$ discussed for the case of prolate condensates. But the coefficient $B_2(\kappa,\mu)$ becomes zero at some critical value of the anisotropy parameter,

$$\kappa_c(\mu) = 2 - \mathcal{O}(1/\ln(\mu)).$$

Hence, the latter instability associated with $m = 2$ does depend on the specific value of the chemical potential, as illustrated in [49], reaching the asymptotic limit of $\kappa_c = 2$ only as $\mu \to \infty$.

Appendix C: Approximate Description of Nonlinear Parametric Instability

Here we give a simplified description of the relevant instability via a fully integrable Hamiltonian with just three degrees of freedom,

$$\begin{aligned} H_{\rm prm} &= (\delta - 2\omega_2)|\mathsf{a}_0|^2 + \omega_2(|\mathsf{a}_2|^2 + |\mathsf{a}_{-2}|^2) \\ &+ U(\mathsf{a}_0^*\mathsf{a}_2^*\mathsf{a}_{-2}^* + \mathsf{a}_0\mathsf{a}_2\mathsf{a}_{-2}), \end{aligned} \tag{C1}$$

where δ is a small detuning parameter. The width of the resonance depends on δ and on the initial wave amplitudes. The growth of the amplitudes is not exponential in time. In particular, with $\delta = 0$ there is a simple solution of the following form,

$$\mathsf{a}_2 = \mathsf{a}_{-2} = \frac{\mathsf{i}\exp(-\mathsf{i}\omega_2 t)}{U(t_0 - t)}, \quad \mathsf{a}_0 = \frac{\mathsf{i}\exp(2\mathsf{i}\omega_2 t)}{U(t_0 - t)}. \tag{C2}$$

This demonstrates a power-law growth and is, in principle, associated with a finite-time singularity, although the dynamics saturates prior to such an event. To analyze the system (C1) in general, one has to take into account the two additional integrals of motion,

$$|\mathsf{a}_0|^2 - |\mathsf{a}_2|^2 = D_+, \qquad |\mathsf{a}_0|^2 - |\mathsf{a}_{-2}|^2 = D_-. \tag{C3}$$

Let us introduce a new canonical complex variable $\mathsf{c} = |\mathsf{a}_0|\exp[\mathsf{i}(\mathrm{Arg}(\mathsf{a}_0) + \mathrm{Arg}(\mathsf{a}_2) + \mathrm{Arg}(\mathsf{a}_{-2}))]$. Accordingly, the dynamical system (C1) is reduced to just one degree of freedom, with an effective Hamiltonian

$$H_{\rm eff} = \delta|\mathsf{c}|^2 + U\sqrt{(|\mathsf{c}|^2 - D_+)(|\mathsf{c}|^2 - D_-)}(\mathsf{c}^* + \mathsf{c}). \tag{C4}$$

The phase trajectories are level contours for the above expression in coordinates $\xi = \mathrm{Re}(\mathsf{c})$ and $\eta = \mathrm{Im}(\mathsf{c})$. In particular, with $D_+ = D_- = D$ we have the family of cubic curves

$$(\xi^2 + \eta^2 - D)(\delta/U + 2\xi) = \text{const}. \tag{C5}$$

The above-mentioned analytic solution corresponds to $\delta = 0$ and $\xi = 0$.

The fully nonlinear three-dimensional system of coupled Gross-Pitaevskii equations behaves, as may be expected, in a more complicated manner. For instance, when shifted from the exact resonance condition sufficiently far by δ, it may demonstrate a recurrent behavior. However, an accurate theoretical description of the recurrence is impossible without taking into account the terms from the four-wave Hamiltonian $\mathcal{H}^{(4)}_v$ and higher orders. The above simplified three-wave model is only valid at an initial low-amplitude stage (as discussed also above), while the recurrence actually occurs at considerably larger wave amplitudes, when the higher order nonlinear terms dominate the dynamics.

[1] C. J. Pethick and H. Smith, *Bose-Einstein Condensation in Dilute Gases* (Cambridge University Press, Cambridge, United Kingdom, 2002).

[2] S. Stringari and L. Pitaevskii, *Bose-Einstein Condensation* (Oxford University Press, Oxford, United Kingdom, 2003).

[3] P. G. Kevrekidis, D. J. Frantzeskakis, and R. Carretero-González, *The Defocusing Nonlinear Schrödinger Equation: From Dark Solitons to Vortices and Vortex Rings* (SIAM, Philadelphia, 2015).

[4] A. L. Fetter and A. A. Svidzinsky, *Vortices in a trapped dilute Bose-Einstein condensate*, Journal of Physics: Condensed Matter **13**, R135 (2001).

[5] A. L. Fetter, *Rotating trapped Bose-Einstein condensates*, Rev. Mod. Phys. **81**, 647 (2009).

[6] S. Komineas, *Vortex rings and solitary waves in trapped Bose–Einstein condensates*, The European Physical Journal Special Topics **147**, 133 (2007).

[7] K.-P. Marzlin, W. Zhang, and B. C. Sanders, *Creation of skyrmions in a spinor Bose-Einstein condensate*, Phys. Rev. A **62**, 013602 (2000).

[8] T. Mizushima, K. Machida, and T. Kita, *Mermin-Ho vortex in ferromagnetic spinor Bose-Einstein condensates*, Phys. Rev. Lett. **89**, 030401 (2002).

[9] J. W. Reijnders, F. J. M. Van Lankvelt, K. Schoutens, and N. Read, *Rotating spin-1 bosons in the lowest Landau level*, Phys. Rev. A **69**, 023612 (2004).

[10] T. Ollikainen, K. Tiurev, A. Blinova, W. Lee, D. S. Hall, and M. Möttönen, *Experimental Realization of a Dirac Monopole through the Decay of an Isolated Monopole*, Phys. Rev. X **7**, 021023 (2017).

[11] D. S. Hall, M. W. Ray, K. Tiurev, E. Ruokokoski, A. H. Gheorghe, and M. Möttönen, *Tying quantum knots*, Nat. Phys. **12**, 478 (2016).

[12] W. Lee, A. H. Gheorghe, K. Tiurev, T. Ollikainen, M. Möttönen, and D. S. Hall, *Synthetic electromagnetic knot in a three-dimensional skyrmion*, Science Advances **4** (2018).

[13] V. P. Ruban, *Three-Dimensional Numerical Simulation of Long-Lived Quantum Vortex Knots and Links in a Trapped Bose Condensate*, JETP Letters **108**, 605 (2018).

[14] C. Ticknor, V. P. Ruban, and P. G. Kevrekidis, *Quasistable quantum vortex knots and links in anisotropic harmonically trapped Bose-Einstein condensates*, Phys. Rev. A **99**, 063604 (2019).

[15] P. G. Kevrekidis and D. J. Frantzeskakis, *Solitons in coupled nonlinear Schrödinger models: A survey of recent developments*, Reviews in Physics **1**, 140 (2016).

[16] Y. Kawaguchi and M. Ueda, *Spinor Bose-Einstein condensates*, Physics Reports **520**, 253 (2012).

[17] D. M. Stamper-Kurn and M. Ueda, *Spinor Bose gases: Symmetries, magnetism, and quantum dynamics*, Rev. Mod. Phys. **85**, 1191 (2013).

[18] M. Trippenbach, K. Góral, K. Rzazewski, B. Malomed, and Y. B. Band, *Structure of binary Bose-Einstein condensates*, J. Phys. B: At. Mol. and Opt. Phys **33**, 4017 (2000).

[19] R. A. Barankov, *Boundary of two mixed Bose-Einstein condensates*, Phys. Rev. A **66**, 013612 (2002).

[20] K. L. Lee, N. B. Jørgensen, I.-K. Liu, L. Wacker, J. J. Arlt, and N. P. Proukakis, *Phase separation and dynamics of two-component Bose-Einstein condensates*, Phys. Rev. A **94**, 013602 (2016).

[21] J. O. Indekeu, C.-Y. Lin, N. Van Thu, B. Van Schaeybroeck, and T. H. Phat, *Static interfacial properties of Bose-Einstein-condensate mixtures*, Phys. Rev. A **91**, 033615 (2015).

[22] K. Sasaki, N. Suzuki, D. Akamatsu, and H. Saito, *Rayleigh-Taylor instability and mushroom-pattern formation in a two-component Bose-Einstein condensate*, Phys. Rev. A **80**, 063611 (2009).

[23] S. Gautam and D. Angom, *Rayleigh-Taylor instability in binary condensates*, Phys. Rev. A **81**, 053616 (2010).

[24] T. Kadokura, T. Aioi, K. Sasaki, T. Kishimoto, and H. Saito, *Rayleigh-Taylor instability in a two-component Bose-Einstein condensate with rotational symmetry*, Phys. Rev. A **85**, 013602 (2012).

[25] H. Takeuchi, N. Suzuki, K. Kasamatsu, H. Saito, and M. Tsubota, *Quantum Kelvin-Helmholtz instability in phase-separated two-component Bose-Einstein condensates*, Phys. Rev. B **81**, 094517 (2010).

[26] N. Suzuki, H. Takeuchi, K. Kasamatsu, M. Tsubota, and H. Saito, *Crossover between Kelvin-Helmholtz and counter-superflow instabilities in two-component Bose-Einstein condensates*, Phys. Rev. A **82**, 063604 (2010).

[27] A. W. Baggaley and N. G. Parker, *Kelvin-Helmholtz instability in a single-component atomic superfluid*, Phys. Rev. A **97**, 053608 (2018).

[28] K. Sasaki, N. Suzuki, and H. Saito, *Capillary instability in a two-component Bose-Einstein condensate*, Phys. Rev. A **83**, 053606 (2011).

[29] J. O. Indekeu, N. Van Thu, C.-Y. Lin, and T. H. Phat, *Capillary-wave dynamics and interface structure modulation in binary Bose-Einstein condensate mixtures*, Phys. Rev. A **97**, 043605 (2018).

[30] A. Bezett, V. Bychkov, E. Lundh, D. Kobyakov, and M. Marklund, *Magnetic Richtmyer-Meshkov instability in a two-component Bose-Einstein condensate*, Phys. Rev. A **82**, 043608 (2010).

[31] C. K. Law, C. M. Chan, P. T. Leung, and M.-C. Chu, *Critical velocity in a binary mixture of moving Bose condensates*, Phys. Rev. A **63**, 063612 (2001).

[32] V. I. Yukalov and E. P. Yukalova, *Stratification of moving multicomponent Bose-Einstein condensates*, Laser Physics Letters **1**, 50 (2004).

[33] H. Takeuchi, S. Ishino, and M. Tsubota, *Binary Quantum Turbulence Arising from Countersuperflow Instability in Two-Component Bose-Einstein Condensates*, Phys. Rev. Lett. **105**, 205301 (2010).

[34] C. Hamner, J. J. Chang, P. Engels, and M. A. Hoefer, *Generation of Dark-Bright Soliton Trains in Superfluid-Superfluid Counterflow*, Phys. Rev. Lett. **106**, 065302 (2011).

[35] H. Saito, Y. Kawaguchi, and M. Ueda, *Ferrofluidity in a Two-Component Dipolar Bose-Einstein Condensate*, Phys. Rev. Lett. **102**, 230403 (2009).

[36] R. N. Bisset, W. Wang, C. Ticknor, R. Carretero-González, D. J. Frantzeskakis, L. A. Collins, and P. G. Kevrekidis, *Robust vortex lines, vortex rings, and hopfions in three-dimensional Bose-Einstein condensates*, Phys. Rev. A **92**, 063611 (2015).

[37] W. Wang, R. N. Bisset, C. Ticknor, R. Carretero-González, D. J. Frantzeskakis, L. A. Collins, and P. G. Kevrekidis, *Single and multiple vortex rings in three-dimensional Bose-Einstein condensates: Existence, stability, and dynamics*, Phys. Rev. A **95**, 043638 (2017).

[38] R. N. Bisset, W. Wang, C. Ticknor, R. Carretero-González, D. J. Frantzeskakis, L. A. Collins, and P. G. Kevrekidis, *Bi-*

furcation and stability of single and multiple vortex rings in three-dimensional Bose-Einstein condensates, Phys. Rev. A **92**, 043601 (2015).

[39] V. P. Ruban, *Parametric instability of oscillations of a vortex ring in a z-periodic Bose condensate and return to the initial state*, J. Exp. Theor. Phys. Lett. **106**, 223 (2017).

[40] B. P. Anderson, P. C. Haljan, C. E. Wieman, and E. A. Cornell, *Vortex Precession in Bose-Einstein Condensates: Observations with Filled and Empty Cores*, Phys. Rev. Lett. **85**, 2857 (2000).

[41] K. J. H. Law, P. G. Kevrekidis, and L. S. Tuckerman, *Stable Vortex–Bright-Soliton Structures in Two-Component Bose-Einstein Condensates*, Phys. Rev. Lett. **105**, 160405 (2010).

[42] M. Pola, J. Stockhofe, P. Schmelcher, and P. G. Kevrekidis, *Vortex–bright-soliton dipoles: Bifurcations, symmetry breaking, and soliton tunneling in a vortex-induced double well*, Phys. Rev. A **86**, 053601 (2012).

[43] S. Hayashi, M. Tsubota, and H. Takeuchi, *Instability crossover of helical shear flow in segregated Bose-Einstein condensates*, Phys. Rev. A **87**, 063628 (2013).

[44] V. P. Ruban, *Instabilities of a Filled Vortex in a Two-Component Bose-Einstein Condensate*, JETP Lett. **113**, 532 (2021).

[45] V. P. Ruban, *Bubbles with attached quantum vortices in trapped binary Bose-Einstein condensates*, J. Exp. Theor. Phys. **133**, 779 (2021).

[46] A. Richaud, V. Penna, R. Mayol, and M. Guilleumas, *Vortices with massive cores in a binary mixture of Bose-Einstein condensates*, Phys. Rev. A **101**, 013630 (2020).

[47] A. Richaud, V. Penna, and A. L. Fetter, *Dynamics of massive point vortices in a binary mixture of Bose-Einstein condensates*, Phys. Rev. A **103**, 023311 (2021).

[48] W. Wang, *Controlled engineering of a vortex-bright soliton dynamics using a constant driving force* (2021), arXiv preprint arXiv:2107.08247.

[49] C. Ticknor, W. Wang, and P. G. Kevrekidis, *Spectral and dynamical analysis of a single vortex ring in anisotropic harmonically trapped three-dimensional Bose-Einstein condensates*, Phys. Rev. A **98**, 033609 (2018).

[50] T.-L. Horng, S.-C. Gou, and T.-C. Lin, *Bending-wave instability of a vortex ring in a trapped Bose-Einstein condensate*, Phys. Rev. A **74**, 041603 (2006).

[51] H. Pu and N. P. Bigelow, *Properties of Two-Species Bose Condensates*, Phys. Rev. Lett. **80**, 1130 (1998).

[52] M. Egorov, B. Opanchuk, P. Drummond, B. V. Hall, P. Hannaford, and A. I. Sidorov, *Measurement of s-wave scattering lengths in a two-component Bose-Einstein condensate*, Phys. Rev. A **87**, 053614 (2013).

[53] S. Lannig, C.-M. Schmied, M. Prüfer, P. Kunkel, R. Strohmaier, H. Strobel, T. Gasenzer, P. G. Kevrekidis, and M. K. Oberthaler, *Collisions of Three-Component Vector Solitons in Bose-Einstein Condensates*, Phys. Rev. Lett. **125**, 170401 (2020).

[54] E. Timmermans, *Phase Separation of Bose-Einstein Condensates*, Phys. Rev. Lett. **81**, 5718 (1998).

[55] P. Ao and S. T. Chui, *Binary Bose-Einstein condensate mixtures in weakly and strongly segregated phases*, Phys. Rev. A **58**, 4836 (1998).

[56] S. B. Papp, J. M. Pino, and C. E. Wieman, *Tunable Miscibility in a Dual-Species Bose-Einstein Condensate*, Phys. Rev. Lett. **101**, 040402 (2008).

[57] T. Busch and J. R. Anglin, *Dark-Bright Solitons in Inhomogeneous Bose-Einstein Condensates*, Phys. Rev. Lett. **87**, 010401 (2001).

[58] V. P. Ruban, *Slow inviscid flows of a compressible fluid in spatially inhomogeneous systems*, Phys. Rev. E **64**, 036305 (2001).

[59] V. P. Ruban, *Stable and Unstable Vortex Knots in a Trapped Bose Condensate*, J. Exp. Theor. Phys. **126**, 397 (2018).

[60] J. Ponstein, *Instability of rotating cylindrical jets*, Appl. Sci. Res. **8**, 425 (1959).

[61] B. Van Schaeybroeck, *Interface tension of Bose-Einstein condensates*, Phys. Rev. A **78**, 023624 (2008).

[62] L. Pitaevskii and S. Stringari, *Bose–Einstein Condensation* (Oxford University Press, Oxford, UK, 2003).

[63] W. Wang, P. G. Kevrekidis, R. Carretero-González, and D. J. Frantzeskakis, *Dark spherical shell solitons in three-dimensional Bose-Einstein condensates: Existence, stability, and dynamics*, Phys. Rev. A **93**, 023630 (2016).

[64] W. Wang and P. G. Kevrekidis, *Two-component dark-bright solitons in three-dimensional atomic Bose-Einstein condensates*, Phys. Rev. E **95**, 032201 (2017).

[65] R. Kollr and R. L. Pego, *Spectral Stability of Vortices in Two-Dimensional Bose-Einstein Condensates via the Evans Function and Krein Signature*, Applied Mathematics Research eXpress **2012**, 1 (2011), ISSN 1687-1200.

[66] Please see the relevant movie: https://www.youtube.com/watch?v=2MOc4o_Zn14.

[67] Please see the relevant movie: https://www.youtube.com/watch?v=oLbMDMiPUQY.

[68] N. Boullé, E. G. Charalampidis, P. E. Farrell, and P. G. Kevrekidis, *Deflation-based identification of nonlinear excitations of the three-dimensional Gross-Pitaevskii equation*, Phys. Rev. A **102**, 053307 (2020).

[69] V. P. Ruban, *Dynamics of straight vortex filaments in a Bose-Einstein condensate with the Gaussian density profile*, J. Exp. Theor. Phys. **124**, 932 (2017).